THE EFFECTS OF LIPID COMPOSITION AND EXTRUSION PRESSURE AND TEMPERATURE ON THE PROPERTIES OF PHOSPHOLIPID VESICLES

by

David Gregory Hunter

B.Sc., University of New Brunswick, 1994

A THESIS SUBMITTED IN PARTIAL FULFILLMENT
OF THE REQUIREMENTS FOR THE DEGREE OF
MASTER OF SCIENCE
in the Department
of
Physics

SIMON FRASER UNIVERSITY
August 1997

Abstract

The production of vesicles, spherical shells formed from lipid bilayers, is an important aspect of recent application of these systems to drug delivery technologies. One popular production method involves pushing a lipid suspension through the cylindrical pores of polycarbonate filters. However, the actual mechanism by which the polydisperse, multilamellar lipid suspension breaks up into a relatively monodisperse population of vesicles is not well understood. We have characterized vesicles produced under different extrusion parameters and from different lipids. We find that the extruded vesicles are only produced above a certain threshold extrusion pressure and have sizes which depend on the extrusion pressure. The flowrate of lipid solutions of concentrations of 1 mg/mℓ through the pores, after being corrected for the viscosity of water, is independent of lipid properties. The minimum pressure appears to be associated with the lysis tension of the lipid bilayer rather than any bending modulus of the system.

Acknowledgments

First, I would like to thank my supervisor, Dr. Barbara Frisken, for her guidance over the past three years. I have learned a great deal from her, about physics and otherwise.

Second, I would also like to thank the other two members of my committee, Dr. Michael Wortis and Dr. Jenifer Thewalt, and Drs. Michael Plischke, David Boal and Art Bailey, my friends Andrew McConnell, Tracey Copeland, Michael Lamont and Charles Asman, as well as a myriad of other people for taking the time to talk to me about my work, and for their help with the umpteen million problems that arose during my research.

Finally, I want to apologise to my wife, Susan, for whom the writing of this thesis has been at least as difficult as it has been for me. Her patience and love have sustained me when I thought I could not carry on. Thank-you.

Dedication

To Susan and Rachael.

Contents

List of Tables

List of Figures

Chapter 1

Introduction

The method of preparing samples of large (> 100 nm) unilamellar vesicles by extrusion through small pores [1] is widely used in research and pharmaceutical applications. In this process, solutions containing extremely large ($\geq$ 1 μm), multi-lamellar vesicles are forced or extruded through pores with diameters on the order of 100 nm using either a pressurized gas [1] or a syringe-based plunger system [2].

While the method of production is in common use, the current state of understanding of the actual mechanism by which the large, polydisperse multilamellar vesicles break up into smaller, unimodal distributions of vesicles is poor. Description of this mechanism should lead to an understanding of why various factors including extrusion parameters and lipid properties affect the size and polydispersity of the extruded samples. Several recent theoretical studies have examined vesicles in pores or under shear. A possible mechanism for vesicle formation hypothesized recently by Clerc and Thompson [3] is based on the breakup of the cylindrical phospholipid bilayer structures of radius R outside the pores into smaller cylindrical structures of length λ, where $\lambda = 2\pi R$ which then reform into vesicles. However, this leads in general to vesicles which are larger than those observed and does not account for variations of vesicle size with extrusion pressure or lipid properties. Gompper and Kroll [4] look at the mobility of vesicles in pores as a function of a driving field. The model vesicles considered are larger than the pore diameter and must deform to enter the pore. Deformation is assumed to be governed by bending energy only. Bruinsma [5] focuses

on the flow of vesicles after they have entered the pore and shape deformations which might occur in the pore. Kraus *et al.* [6] study vesicle deformation as a result of applying shear, but the situation examined does not apply directly to the problem of extrusion. Of these studies, only that of Clerc and Thompson takes the possible rupture of the vesicles into account, a necessary condition for the understanding of extrusion.

We have prepared vesicles composed of several types of phospholipids by extrusion through polycarbonate filters at a constant concentration of 1 mg/mℓ. The volume flowrate of these samples and the number of times the sample was extruded to achieve a constant flowrate was measured for each sample. The size and polydispersity of the samples were measured using dynamic and static light scattering techniques. It was observed that there is a minimum pressure required to force vesicles through the polycarbonate filters below which extrusion was not possible. The size of the extruded vesicles was dependent on the extrusion pressure. The flowrate of the vesicle suspensions through the filters did not depend on the lipid properties. We conclude that the minimum pressure is a function of the lysis tension of the vesicles rather than the bending modulus of the lipid bilayer.

Summarizing the contents of this thesis, Chapter 2 discusses the theory of light scattering, including dynamic and static light scattering techniques and the analysis of data from such experiments. Chapter 3 includes a basic description of phospholipids and vesicles, then goes on to look at the production of vesicles by extrusion and current ideas of the method of vesicle formation by this technique. In Chapter 4, the experimental apparatus, materials, and procedure are described. The experimental results are also described in Chapter 4. The discussion and analysis of the results are presented in Chapter 5. Chapter 6 summarises the results and suggests directions for future experiments.

Chapter 2

Laser Light Scattering Theory and Techniques

This chapter assumes that the reader has at least a passing familiarity with the fundamentals of electromagnetic radiation and its interaction with matter. Because of this, several equations and relations will be introduced without derivation. For readers needing to learn or refresh their knowledge of electromagnetism, I recommend "Electromagnetic Field Theory" by Jack Vanderlinde [7]. An overview of light scattering can be found in Johnson and Gabriel [8]. Basic dynamic light scattering theory is covered by Berne and Pecora [9].

As a further note to the reader, all the results here have been developed with the assumption that the scatterers are small compared to the wavelength of light and isotropic. That is, the theory has been developed with scattering from spherical vesicles already in mind.

2.1 Electromagnetic Field Theory

The physical arrangement of a typical laser light scattering experiment is shown in Fig. 2.1. A beam of laser light is directed through the scattering cell, where a portion of this light is scattered in directions other than the forward one. A detector placed at position $\mathbf{R}$ measures the intensity of the scattered light at that position. The volume

defined by the overlap of the scattered beam and the incident beam is referred to as the scattering volume. Only the electric field of the propagating electromagnetic wave of light will be considered here, as the strength of its interaction with matter is much greater than that of the magnetic field. We will assume that the incident laser light is a plane wave, with an electric field

$$\mathbf{E}_i(\mathbf{r},t) = E_o\hat{\mathbf{n}}_i \exp(i\mathbf{k}_i\cdot\mathbf{r})\exp(i\omega_i t)\ , \tag{2.1}$$

where the magnitude of the field is E_o, $\hat{\mathbf{n}}_i$ denotes the direction of polarization of the field, and ω_i is the angular frequency of the field. The direction of propagation is given by the wave vector $\mathbf{k}_i$. The magnitude of the wave vector $|\mathbf{k}_i| = 2\pi n/\lambda$, where λ is the wavelength of the incident light in vacuo and n is the index of refraction of the medium.

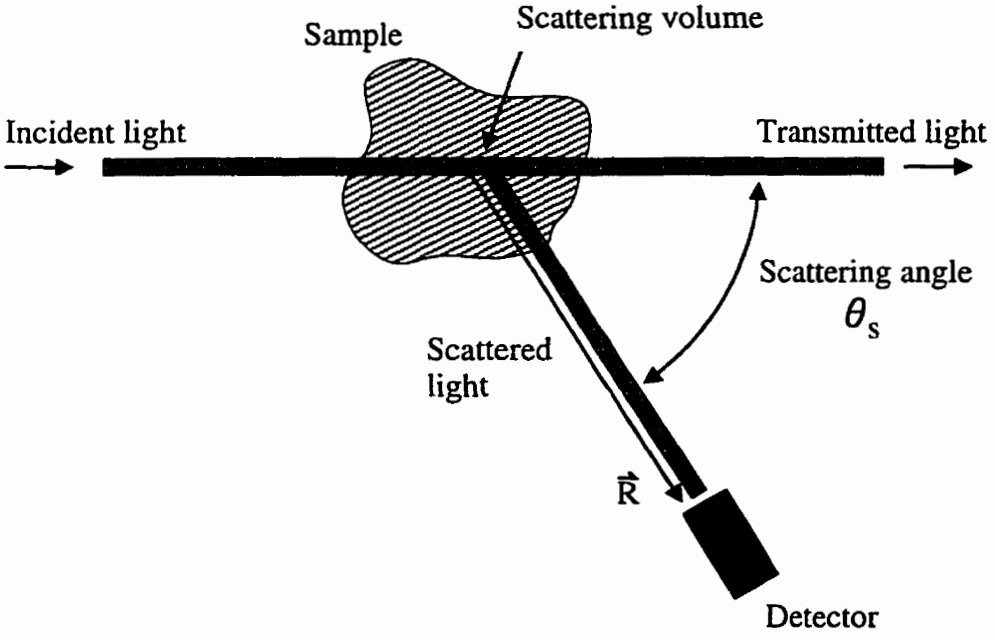

Figure 2.1: A diagram of the arrangement of a light scattering experiment.

Light travelling through a dielectric medium is scattered because the electromagnetic field of the incident light accelerates the charges in the scattering volume. These accelerated charges form oscillating dipoles with frequency ω_i. The general expression

for the induced dipole is

$$\mathbf{P} = \underline{\alpha}\cdot\mathbf{E} \,, \tag{2.2}$$

where $\underline{\alpha}$ is the polarizability tensor.[1] In general, $\mathbf{P}$ is not necessarily in the same direction as $\mathbf{E}$. However, for scatterers with isotropic polarizability, there is no depolarization of the incident light, and $\mathbf{P}$ is in the same direction as $\mathbf{E}$.

Electromagnetic theory says that an oscillating dipole emits radiation. It can be shown that at a position R far from the dipole, where $R \gg \lambda$, the radiated field is proportional to $d^2\mathbf{P}/dt^2$. For gases, this results in a scattered field that is proportional to the inverse square of the wavelength, λ, and to the polarizability α. Since the intensity of light is

$$I = c\varepsilon_o|\mathbf{E}|^2 \,, \tag{2.3}$$

where c is the speed of light *in vacuo*, the intensity of the scattered light is inversely proportional to the fourth power of the wavelength, as first shown by Lord Rayleigh.

The situation is not quite so simple for scattering from condensed phases of matter. In these media, the intensity of scattered light can be reduced because of destructive interference. For example, for every point in a uniform medium it is always possible to find another point whose scattered field at the detector is 180° out of phase with that of the first point and equal in amplitude, resulting in complete destructive interference and no scattered light. Variations in the dielectric constant can change the amplitudes of the scattered field so that the sum is not zero. For example, light can only be scattered from a crystalline solid when the Bragg condition $\sin(\theta_s/2) = n\lambda/2d$, where d is the distance separating scattering planes, is satisfied. Wavelengths that are much larger than d are not scattered, but those λ which are comparable to d are scattered at the angle specified by the Bragg relation. Thus, crystals have a dielectric constant which varies regularly in space.

In liquid phases, the scattering centres are not stationary, but move about randomly as they undergo Brownian motion. The dielectric constant of the medium

[1] It can be shown from electromagnetic field theory that $\underline{\varepsilon} = \varepsilon_o\underline{\mathbf{I}} + \underline{\alpha}$, where $\underline{\alpha}$ is the polarizability tensor of a medium with dielectric constant $\underline{\varepsilon}$ and ε_o is the permittivity of free space. Thus, the polarizability differs from the dielectric constant by a constant only. Furthermore, it follows from this that $\delta\underline{\varepsilon} = \delta\underline{\alpha}$. That is, the dielectric fluctuations are identical to the polarizability fluctuations. I will therefore use $\delta\underline{\varepsilon}$ and $\delta\underline{\alpha}$ interchangably.

fluctuates in space and time and can be written

$$\underline{\varepsilon} = \varepsilon \underline{\mathbf{I}} + \delta\underline{\varepsilon}(\mathbf{r}, t) \ , \tag{2.4}$$

where ε is the average dielectric constant of the medium, $\delta\underline{\varepsilon}(\mathbf{r}, t)$ is the dielectric fluctuation tensor at position $\mathbf{r}$ and time t, and $\underline{\mathbf{I}}$ is the second-rank unit tensor. The exact form of the scattered field depends on the physical characteristics of the system under examination and on the arrangement of the experimental apparatus. Only two relevant cases will be considered here, those regarding the time averaged intensity and the time-correlated intensity fluctuations. In both cases, the size of the particle that is being studied is smaller than the wavelength of light in the medium, but larger than approximately $\lambda/10$.

2.1.1 Static Light Scattering

As shown in Appendix A, the magnitude of the component of the scattered electric field with polarization $\mathbf{n}_f$ and frequency ω_f propagating in direction $\mathbf{k}_f$ is

$$E_s(R, t) = \frac{E_o}{4\pi\varepsilon_o R} \exp\left[i(k_f R - \omega_i t)\right] \int_V d^3r e^{i\mathbf{q}\cdot\mathbf{r}} \mathbf{n}_f \cdot [\mathbf{k}_f \times \mathbf{k}_f \times [\delta\underline{\varepsilon}(\mathbf{r}, t) \cdot \hat{\mathbf{n}}_i]] \ . \tag{2.5}$$

The volume integral is taken over the entire scattering volume. The scattering angle θ_s and the incident wave vector $\mathbf{k}_i$ together define the scattering wave vector $\mathbf{q}$. These quantities are illustrated in Fig. 2.2. The scattering wave vector is the difference between the wave vectors of the incident and scattered light, i.e., $\mathbf{q} = \mathbf{k}_i - \mathbf{k}_f$, where $\mathbf{k}_f$ points from the scattering volume to the detector. In general, $\mathbf{k}_i$ and $\mathbf{k}_f$ are not necessarily of the same magnitude. However, most light scattering experiments are conducted at wavelengths far from resonances of the sample. The wavelength of the scattered light is not significantly different from that of the incident light, in which case $|\mathbf{k}_i| = |\mathbf{k}_f|$. The magnitude of the scattering wave vector $\mathbf{q}$ is then

$$|\mathbf{q}| = |\mathbf{k}_i - \mathbf{k}_f| \cong \frac{4\pi n}{\lambda} \sin(\theta_s/2) \ . \tag{2.6}$$

The scattered wave vector $\mathbf{q}$ is inversely proportional to the size of the object or the wavelength of the fluctuation which is probed using light scattering. By varying the wavelength or the scattering angle, the size of features probed is changed.

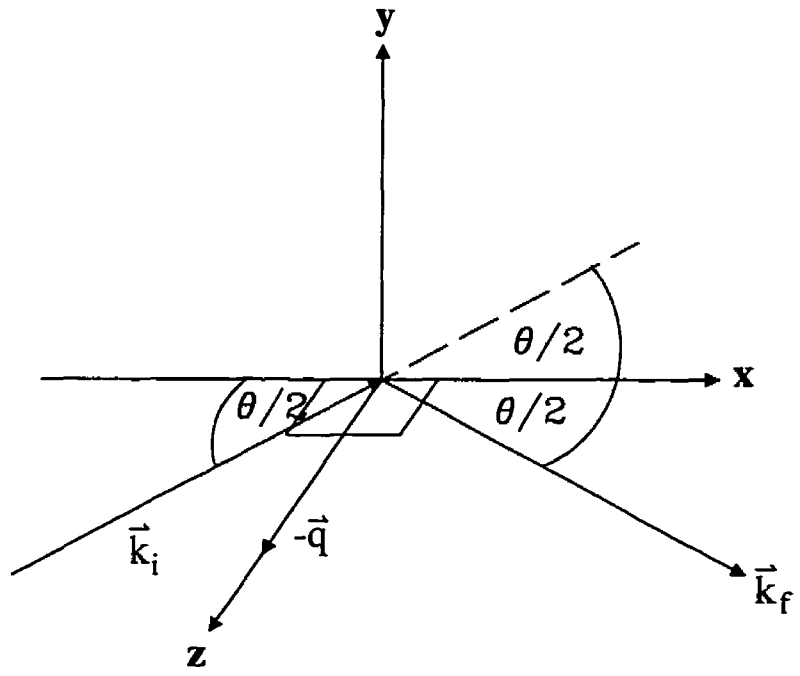

Figure 2.2: Vector diagram of geometry of scattering experiment

Equation 2.5 can be simplified by replacing the dielectric fluctuation tensor with its spatial Fourier transform

$$\delta\underline{\varepsilon}(\mathbf{q},t) = \int_V d^3r e^{i\mathbf{q}\cdot\mathbf{r}} \delta\underline{\varepsilon}(\mathbf{r},t) \ , \tag{2.7}$$

and working out the cross products, so that

$$E_s(r,t) = \frac{-k_f^2 E_o}{4\pi\varepsilon_o R} \exp\left[i(k_f R - \omega_i t)\right] \delta\varepsilon_{if}(\mathbf{q},t) \ , \tag{2.8}$$

where

$$\delta\varepsilon_{if}(\mathbf{q},t) \equiv \hat{\mathbf{n}}_f \cdot \delta\underline{\varepsilon}(\mathbf{q},t) \cdot \hat{\mathbf{n}}_i \ . \tag{2.9}$$

This simplification requires the use of the vector identity $\mathbf{a}\times(\mathbf{b}\times\mathbf{c}) = (\mathbf{a}\cdot\mathbf{c})\mathbf{b} - (\mathbf{a}\cdot\mathbf{b})\mathbf{c}$ and the fact that the direction of polarization of light must be perpendicular to the direction of propagation, that is, $\hat{\mathbf{n}}_f \cdot \mathbf{k}_f = 0$. It should also be noted that, since there is no change in the direction of polarization of the light for isotropic scatterers, $\hat{\mathbf{n}}_f$ and $\hat{\mathbf{n}}_i$ are parallel and $\hat{\mathbf{n}}_f \cdot \delta\underline{\varepsilon}(\mathbf{q},t) \cdot \hat{\mathbf{n}}_i = \delta\varepsilon_{ii}(\mathbf{q},t)$.

Although the electric field of the scattered light has been derived, this is not what is measured experimentally. Light detectors (most commonly photomultiplier tubes in light scattering experiments) measure the intensity of light incident on the detector. The instantaneous intensity of the scattered light is related to the electric field by Eq. 2.3. The cycle-averaged, or time-averaged, intensity is equal to 1/2 the instantaneous intensity, so the time-averaged scattered intensity and incident intensity are, respectively,

$$I_s = \frac{c\varepsilon_o}{2}\frac{k_f^4 E_o^2 \overline{(\delta\varepsilon_{ii}(\mathbf{q}))^2}}{16\pi^2\varepsilon_o^2 R^2} , \tag{2.10}$$

and

$$I_i = \frac{c\varepsilon_o}{2}E_o^2 , \tag{2.11}$$

where $\overline{(\delta\varepsilon_{ii}(\mathbf{q}))^2}$ is the cycle average of the square of the dielectric fluctuations. The other term, the square of the average of the fluctuations, is identically equal to zero. The ratio of the scattered intensity to the incident intensity is

$$\frac{I_s}{I_i} = \frac{\pi^2 \overline{(\delta\varepsilon_{ii}(\mathbf{q}))^2} n^4}{\lambda^4 \varepsilon_o^2 R^2} . \tag{2.12}$$

Thus, the time-averaged scattered intensity is a source of information on the mean square polarizability fluctuations in the sample. The observed scattered intensity is inversely proportional to λ^4, as is expected. Note that this assumes that the scatterers are much smaller than the wavelength of the laser light. If this were not the case, the phase of the light wave would vary significantly over the scatterer, and the derivation of Appendix A would be invalid, instead requiring the use of the more involved Mie theory.

TThe criterion for the validity of the Rayleigh-Gans-Debye approximation is

$$\frac{4\pi}{\lambda} R\,|m-1| \ll 1 , \tag{2.13}$$

where λ is the wavelength of light *in vacuo*, R is a characteristic dimension of the particle, and m is the ratio of the refractive index of the particle to that of the suspending medium. As just stated above, this relation implies that the phase of a light wave crossing the particle is not significantly changed by the particle. This

approximation breaks down when the diameter of the particle is of the same order of magnitude as the wavelength of light, and when the particle is very different optically from the surrounding medium [9]. Now, our scatterers are smaller than the wavelength of light, being on the order of 100 nm in diameter. However, the ratio of indices of refraction is 1.05. Upon evaluation we find that the left hand side of Eq. 2.13 is 0.13, which is less than 1 so that Rayleigh-Gans theory is appropriate.

Due to the size of the particles, the path difference for light from two points in the scatterer may be large enough to cause measurable interference effects. These will cause a decrease in the scattered intensity. This decrease in intensity varies with the size and shape of the particle, revealing information about these properties of the particles. The dependence of the scattered intensity on these factors is contained in a multiplicative correction factor known as the form factor P(**q**), where

$$P(\mathbf{q}) = \frac{\text{scattered intensity at } \theta_s}{\text{scattered intensity at } \theta_s = 0} \,. \tag{2.14}$$

This assumes that the particles are non-interacting. This condition is true in the limit of low number densities of scatterers. That is, there must be few enough scatterers that they are almost never close enough to interact with each other. This distance, dependent on the Debye length in the solution and the surface charge of the scatterers (among other things), is an experimentally-controllable parameter. (The second condition has been shown to be true for vesicles by Strawbridge *et al* [10].) If the particles do interact with each other, an additional correction $S(\mathbf{q})$, called the structure factor, is necessary. Interacting scatterers can form semi-regular arrangements of particles, similar to a crystal. The result is that a very broad bump will appear in the spectrum corresponding to the average distance of separation of the scattering centres. The broadness of the bump is due to the fact that the scatterers are not stationary, so that the relative intermolecular distance is constantly changing, altering the position of the constructive interference peak in momentum space at the same time. This bump in the spectrum is analagous but not identical to the Bragg peak seen in the scattering spectra of crystals. The information about both $P(\mathbf{q})$ and $S(\mathbf{q})$ is contained in the dielectric fluctuation term $\delta\varepsilon(\mathbf{q}, t)$.

Consideration of the phase difference of light scattered from different points of a

single particle averaged over all orientations of the particle yields the general equation for the form factor [8]:

$$P(\mathbf{q}) = \left\langle \left| \frac{1}{\ell} \sum_{j=1}^{\ell} e^{i\mathbf{q}\cdot\mathbf{r}_j} \right|^2 \right\rangle , \tag{2.15}$$

where ℓ is the number of scattering segments in the particle, $\mathbf{r}_j$ is the position of the jth segment, and the closed brackets denote the average over all orientations. In evaluating Eq. 2.15, some assumptions must be made about the shape of the scattering particle. As will be discussed in Chapter 3, it is reasonable to assume that the vesicles are hollow spheres with some finite thickness. As shown in Appendix B, the form factor for a hollow sphere with outer radius R_o, inner radius R_i and thickness t is

$$P(\mathbf{q}) = \left[\left(\frac{3}{q^3 t^3} \right) (\sin qR_o - qR_o \cos qR_o - \sin qR_i + qR_i \cos qR_i) \right]^2 . \tag{2.16}$$

The inner radius is related to the outer radius by the shell thickness, such that $R_i = R_o - t$. Because the vesicle is spherically symmetric, it is not necessary to average over all the possible orientations in this case. It is important to note that it has been assumed that all of the particles in the scattering volume are identical to one another. If the scatterers are of differing sizes, P(q) becomes a weighted average over R. If the scatterers vary in shape, it is necessary to know the relative numbers of the different shapes, otherwise the problem of calculating the mean form factor becomes intractable. In any event, unless there is some *a priori* knowledge of the population distribution, any polydisperse sample with a mean radius R appears to be a population of monodisperse spheres of some smaller radius. [2]

A typical static light scattering experiment measures the time-averaged intensity of the scattered light as a function of scattering angle. Changing the scattering angle changes the magnitude of the scattering wave vector $\mathbf{q}$, as can be seen from Eq. 2.6. The angular spacing of the measurements varies, with smaller spacing at small angles. This is a direct result of the sine function in the form of $\mathbf{q}$; small changes in θ_s are much more important at small angles. It is of course desirable to have as great a range of angles as possible to maximize the accessible values of $\mathbf{q}$. At each angle

[2]This is due in part to the range of q accessible to our experiments.

the intensity is measured for a specified period of time determined by the photon count rate, the intensity-intensity correlation time to be obtained and the desired level of uncertainty in the measurement's accuracy; the uncertainty in the intensity measurement is proportional to the square root of the number of counts.

The multiplicative $P(\mathbf{q})$ factor has the form of a spherical Bessel function. If at all possible it is also preferable that the ranges of scattering angle overlap a minimum of the Bessel function so as to aid the fitting by providing a fixed reference point. That is, it is desirable to have a minimum of the function within the available range of $\mathbf{q}$ vectors. It also gives the researcher a good idea of the particle size with merely a cursory examination of the data.

The remaining necessary corrections to the intensity spectrum data are due to reflections from interfaces of differing indices of refraction in the sample chamber, e.g., between the containers and the fluids contained therein. The form of these corrections are well known and can be directly incorporated in the data processing[3], along with the Rayleigh ratio factors. The resulting fit to the data has only the parameters of the $P(\mathbf{q})$ function, the outer radius R_o and the vesicle thickness t, as free parameters.

2.1.2 Dynamic Light Scattering

The scattering event is almost but not quite elastic. Any given individual scattered photon will have its frequency Doppler-shifted because the scattering vesicle is moving with some arbitrary velocity $\mathbf{v}$, but the shift is so small that the change in the photon's energy is negligible, hence the term "quasi-elastic." There is some broadening of the spectral line width, but this broadening is very small compared to the frequency of the light $\omega \sim 10^{14}$ Hz. The shift is small because the scattering centres are moving very slowly compared with the time required for a wavelength of light to pass the scatterer. Static light scattering (SLS) uses the time averaged intensity to study the mean-square fluctuations in the polarizability. The SLS experiment simply measures the sum of all the intensity spectrum around the frequency of the incident light ignoring the broadening.

[3]The corrections for reflections in the sample chamber are quite complex. They have not been included here as doing so would not be informative, and might obscure matters.

On the other hand, dynamic light scattering (DLS) actually measures the frequency broadening of the scattered light, the broadening being proportional to the diffusion coefficient of the scatterer(s). While the intensity of light scattered from the scattering volume is the sum of the light scattered by the medium and that scattered by the suspended particles, the density fluctuations in the medium occur in times which are too small to be measured by light scattering techniques[4]. The total scattered field in a DLS experiment is then proportional only to the sum of the field scattered from each suspended particle ℓ in the scattering volume [9],

$$\mathbf{E}_s(\mathbf{q},t) \propto \sum_{\ell=1}^{N} \alpha_\ell e^{i\mathbf{q}\cdot\mathbf{r}_\ell(t)} \ , \tag{2.17}$$

where N is the number of scatterers in the scattering volume, α_ℓ is the average polarization of the ℓth particle, and $\mathbf{r}_\ell$ is the position of the ℓth particle.[5] It is not necessary to consider the constants of proportionality implicit in Eq. 2.17 because, as we will see shortly, we will be normalizing our results to the average scattered fields and intensities, as appropriate.

A normal dynamic light scattering experiment is actually a series of shorter observations which are analysed individually. Each of these shorter observations is conducted at a single scattering angle, at each of which the intensity (actually number of photons counted) is measured as a function of time for a period of time sufficient to reach the desired uncertainty in the measurement. The minimum required length of time t is related to the desired uncertainty Δ by the expression [11]

$$\Delta = 4\sqrt{\frac{1}{Dq^2t}} \ , \tag{2.18}$$

where D is the translational diffusion coefficient (to be discussed shortly) and q is the magnitude of the scattering wave vector $\mathbf{q}$. It will be necessary to consider θ_s as it affects the wave vector $\mathbf{q}$ again during the analysis of the data. Note that there is no variation of the mean scattered intensity due to the constant scattering angle. Only the variation of the intensity as a function of time is of interest.

[4]Such measurements would require the use of an interferometer, which is sensitive to shorter time scales.

[5]For convenience, I have changed from an integral notation to a summation, which is entirely equivalent to Eq. 2.5 within a multiplicative factor.

The variation of the scattered field in Eq. 2.17 on time is implicit; the position vectors $\mathbf{r}_\ell$ are changing as the particles move about randomly in Brownian motion, and this means that the relative position of the scatterers is changing in time. The variation can be well characterized by the first-order time autocorrelation function of the scattered field $G^{(1)}(\tau)$, defined as

$$G^{(1)}(\mathbf{q},\tau) = \langle E^*(\mathbf{q},t)E(\mathbf{q},t+\tau)\rangle = \langle E^*(\mathbf{q},0)E(\mathbf{q},\tau)\rangle \ . \tag{2.19}$$

The field autocorrelation function is the time average of the complex conjugate of the scattered field at a particular $\mathbf{q}$ at time t multiplied by the scattered field at the same $\mathbf{q}$ at some time $t+\tau$ later. The time t can be replaced with zero because the scattered field is varying about an unchanging central value. Hence, $G^{(1)}(\mathbf{q},\tau)$ depends only on the time τ between the field observations, not the time origin. When there is no lag between the two field observations, i.e. τ=0, $G^{(1)}(\mathbf{q},0) = \langle I_s(\mathbf{q})\rangle$, the average value of the scattered intensity. When τ is very large, there is no correlation between $\mathbf{E}_s(\mathbf{q},t)$ and $\mathbf{E}_s(\mathbf{q},t+\tau)$, and $G^{(1)}(\mathbf{q},\infty) \cong \langle \mathbf{E}_s(\mathbf{q},t)\rangle^2 \equiv 0$.

Substituting the form of the scattered field in Eq. 2.17 into Eq. 2.19 gives

$$G^{(1)}(\mathbf{q},\tau) \propto \sum_{\ell,m=1}^{N} \left\langle \alpha_\ell^* \alpha_m e^{i\mathbf{q}\cdot[\mathbf{r}_m(\tau)-\mathbf{r}_\ell(0)]} \right\rangle \ . \tag{2.20}$$

Now, if the motions of the particles are not correlated with each other, and there is no coupling of translational and rotational motions, the summation in Eq. 2.20 collapses to a multiplicative factor of $N = \langle N\rangle$, the mean number of particles in the scattering volume, so that

$$G^{(1)}(\tau) = AN\alpha^2 \left\langle e^{i\mathbf{q}\cdot[\mathbf{r}(\tau)-\mathbf{r}(0)]} \right\rangle \ , \tag{2.21}$$

where A is a constant containing factors such as the field strength and the inverse 4th-power wavelength dependence. It has been assumed that all of the particles have the same polarizability α so that the subscript ℓ is redundant and has been dropped. Since dynamic light scattering experiments are conducted at a single angle, the correlation functions will henceforth be written as function of τ only, it being understood that the $\mathbf{q}$ dependence is implicit. It can be seen that the field autocorrelation function depends on the number of scatterers, their polarizability, and their positions. Note that the

polarizability α given here is the same as the polarizability fluctuation $\delta\alpha \equiv \delta\varepsilon$, i.e., the fluctuations in the otherwise isotropic dielectric medium are due to the suspended particles.

As has been stated previously, light detectors measure the scattered intensity, not the scattered field. More properly, a PMT converts photons to electric current pulses, the number of which is related to the intensity of light by a multiplicative efficiency factor dependent on the tube. A special instrument called a correlator calculates the intensity autocorrelation function $G^{(2)}(\tau)$, defined as

$$G^{(2)}(\tau) = \langle I_s(0) I_s(\tau) \rangle \ . \tag{2.22}$$

In general, $G^{(2)}(\tau)$ is not simply related to $G^{(1)}(\tau)$. However, if the scattered field is a gaussian random variable, that is, the scattered field varies about a mean field in a gaussian distribution, then the Siegert relation [8] states that $G^{(2)}(\tau)$ and $G^{(1)}(\tau)$ are related by

$$G^{(2)}(\tau) = \langle I_s \rangle^2 + |G^{(1)}(\tau)|^2 \ . \tag{2.23}$$

This relation is generally true for suspensions at room temperature and concentrations where number fluctuations of scatterers in the scattering volume are not important. This will always be the case in this study. It is more usual to discuss the normalised correlation functions $g^{(1)}(\tau)$ and $g^{(2)}(\tau)$, defined as

$$g^{(1)}(\tau) = \frac{\langle E_s^*(0) E_s(\tau) \rangle}{\langle E_s^*(0) E_s(0) \rangle} \text{ and} \tag{2.24}$$

$$g^{(2)}(\tau) = \frac{\langle E_s^*(0) E_s(0) E_s^*(\tau) E_s(\tau) \rangle}{\langle E_s^*(0) E_s(0) \rangle^2} \ . \tag{2.25}$$

The actual observed correlation function will have its $g^{(1)^2}(\tau)$ component multiplied by a factor β, which depends on the geometry and apparatus of the experimental setup. Thus, the form of $g^{(2)}(\tau)$ used experimentally is

$$g^{(2)}(\tau) = 1 + \beta |g^{(1)}(\tau)|^2 \ . \tag{2.26}$$

For most purposes of this study, the primary tool of investigation has been dynamic light scattering, with static light scattering used to confirm the DLS results. I will correspondingly put most of the emphasis on dynamic light scattering from this point on.

2.2 Methods of Analysis

The normalised intensity correlation function given in Eq. 2.26 has incorporated no assumptions about the form of $g^{(1)}(\tau)$. The mean of the exponential in Eq. 2.21 can be written as the weighted average of a distribution of exponentials, such that

$$\left\langle e^{i\mathbf{q}\cdot[\mathbf{r}(\tau)-\mathbf{r}(0)]}\right\rangle = \int d\mathbf{R} e^{i\mathbf{q}\cdot[\mathbf{r}(\tau)-\mathbf{r}(0)]} f_s(\mathbf{R},\tau) \ , \tag{2.27}$$

where

$$f_s(\mathbf{R},\tau) = \langle \delta(\mathbf{R} - [\mathbf{r}(\tau) - \mathbf{r}(0)])\rangle \tag{2.28}$$

is the probability distribution giving the location of the particles in the scattering volume. The vesicles under consideration are undergoing Brownian motion, executing random walks through the sample. For times long with respect to the time to complete one of the steps of the random walk, the probability of finding the particle at a distance r from its starting point at a time t later is

$$f_s(r,t) = (4\pi Dt)^{-3/2} e^{r^2/4Dt} \ , \tag{2.29}$$

where D is the diffusion coefficient of the particle. Using Eqs. 2.27 and 2.29 and assuming that all of the particles are the same size, Eq. 2.21 becomes

$$G^{(1)}(\tau) = AN\alpha^2 e^{-Dq^2\tau} \ . \tag{2.30}$$

It can be seen that for particles undergoing Brownian motion, the intensity autocorrelation function $g^{(2)}(\tau)$ is a function of the diffusion coefficient of the particles. In particular, there is a characteristic exponential decay rate, usually denoted as $\Gamma = Dq^2$. The usual form of the diffusion constant is given by the Stokes-Einstein relation,

$$D = \frac{k_B T}{6\pi\eta R_h} \ , \tag{2.31}$$

where η is the viscosity and R_h is the hydrodynamic radius of the particle. Thus, the size of the particles in the scattering volume can be extracted from the intensity autocorrelation function.

2.2.1 Polydispersity

Up to this point, it has been assumed that all of the particles in suspension are the same shape and size. While it is possible to ensure that all of the vesicles are spherical by controlling the osmotic pressure across the bilayer, in general there will not be a single size of vesicle, but a distribution of sizes $\tilde{p}(R_h)$, to which there is a corresponding distribution of decay rates $p(\Gamma)$. The effect on the normalised field autocorrelation function $g^{(1)}(\tau)$ is given by

$$g^{(1)}(\tau) = \int_0^\infty p(\Gamma)\mathrm{e}^{-\Gamma\tau}d\Gamma \ . \tag{2.32}$$

It may be noted that Eq. 2.32 is the Laplace transform of $p(\Gamma)$. Theoretically, it is possible to obtain the distribution of decay rates, and therefore the sizes, by performing a Laplace inversion of the correlation function. Such an inversion, however, requires measurement of virtually the entire range of Γ from 0 to ∞, which is not experimentally possible. The resulting problem is therefore ill-conditioned, and not feasible unless some *a priori* knowledge of $p(\Gamma)$ is incorporated.

The most common method of analysing the correlation function is the method of cumulants proposed by Koppel [12]. Cumulant expansion has the advantages of having a low number of parameters and good convergence and stability of the fitted parameters. Its disadvantage is that use of this expansion assumes that the distribution of Γ is unimodal. The unimodality can be confirmed by using Laplace inversion routines such as CONTIN to check qualitatively for the possibility of multimodal decay rate distributions. In general, the cumulant expansion is defined as

$$\ln g^{(1)}(\tau) = \sum_{n=1}^{\infty} \frac{(-\tau)^n}{n!}\mu_n(\Gamma) \ , \tag{2.33}$$

where μ_n is the nth cumulant. Having $g^{(1)}(\tau)$ of the form in Eq. 2.32 gives the cumulants in terms of the moments of the distribution $< \Gamma^m >$, which are defined by

$$< \Gamma^m >= \int d\Gamma\, \Gamma^m p(\Gamma) \ . \tag{2.34}$$

The first three cumulants of the expansion are then

$$\mu_1(\Gamma) \ = \ < \Gamma > \ ,$$

$$\begin{aligned} \mu_2(\Gamma) &= <\Gamma^2> - <\Gamma>^2 \text{ , and} \\ \mu_3(\Gamma) &= <\Gamma^3> -3<\Gamma><\Gamma^2> +2<\Gamma>^3 \text{ .} \end{aligned} \tag{2.35}$$

With sufficient data, it is possible to fit all of the cumulants, but in general the range of Γ is too short. Luckily, the higher order cumulants are usually small, so that the expansion can be truncated after the first few cumulants. It is obvious that the first cumulant μ_1 is the mean decay rate of the sample. The second cumulant μ_2 is the variance σ^2 of $\langle\Gamma\rangle$, and μ_3 is the skewness of the distribution. The second cumulant divided by the square of the mean decay rate is dimensionless and gives an indication of the polydispersity of the distribution of Γ. It must be noted that this does not necessarily imply any knowledge about the distribution of the sizes implicit in the decay rate. If the third cumulant is also negligible, as it usually is, then the first two cumulants describe a symmetric distribution of decay rates, which is taken to be a gaussian. The distributions $p(\Gamma)$ and $\tilde{p}(R_h)$ are then proportional to one another.

The cumulant expansion has used the assumptions that τ is small and that $p(\Gamma)$ is narrow. For practical purposes, this requires that

$$\frac{\mu_2}{\overline{\Gamma}^2} \leq 0.3 \text{ .} \tag{2.36}$$

The model function that was fitted to the data was obtained by substituting the expansion of $g^{(1)}(\tau)$ with only the first two cumulants into Eq. 2.26, which yields

$$g^{(2)}(\tau) = B + Ae^{-2\overline{\Gamma}\tau+\mu\tau^2} \text{ ,} \tag{2.37}$$

where $\mu = \mu_2$ is the variance of the distribution. It was found that it was not necessary to include higher order terms.

2.2.2 Fitting Algorithm

The intensity correlation model function given in Eq. 2.37 was fit to the data using a C subroutine known as *nllsq*, which stands for Non-Linear Least SQuares, written by A. Kornblit. The *nllsq* routine takes a set of N data points and fits a given model function with adjustable parameters to this . The goodness-of-fit, or merit function

used is the sum of the square of the residuals,

$$\chi^2 = \sum_{i=1}^{N} \left(\frac{(y_i^{data} - y_i^{fit})}{\sigma_i} \right)^2 , \tag{2.38}$$

where y_i^{data} is the ith data point, y_i^{fit} is the fit to the ith data point, and σ_i is the weight of the ith data point. This function is minimised with respect to all model parameters x_j such that the matrix of derivatives vanishes:

$$\frac{\partial \chi^2}{\partial x_j} = 0 . \tag{2.39}$$

The non-linear nature of the model function means that its dependence on its parameters is difficult, if not impossible, to put into a closed form. An approximate solution can be found by iteratively improving the vector of fit parameters from an initial given set of parameter estimates. In each iteration of the fit program, a correction vector is generated from the last set of parameters and added to the fit vector. This correction vector points down the slope of the χ^2 surface in parameter space. The entire process is repeated until some condition for convergence is satisfied. This includes, but is not limited to, having the magnitude of the correction vector less than some (small) preset value.

The *nllsq* routine uses the Marquardt algorithm to search for the minimum in the χ^2 surface. This algorithm varies smoothly between two other algorithms, the Taylor expansion method and the gradient method. The gradient method is useful for rapidly finding the approximate location of the minimum. The Taylor expansion method is suitable for use near the minimum, expanding the surface as quadratic about the minimum. This algorithm is discussed much more completely in Numerical Recipes, by Press *et al* [13].

Chapter 3

Vesicles and Extrusion

The membranes of living organisms are the sites of virtually all biologically important functions and reactions. Correspondingly, they are the focus of much interest and research from the scientific and medical communities. One of the main functions of membranes is to allow only selective transport of certain molecules through them. In particular, ions and large molecules are almost completely prevented from crossing a membrane without assistance of some sort. This allows cells to maintain ionic, concentration and pH gradients across the membrane. One of the ways that this feature of membranes is put to use in living cells is by encapsulating molecules that need to be moved from one point to another inside a closed shell of membrane; this structure is known as a vesicle. The vesicle can then be transported to its destination and the contents released in the proper location.

Artificial versions of membranes and vesicles can be created easily in the laboratory for use as simple model systems. These are created from synthetic or purified natural amphiphiles and contain only those proteins desired. The physics of such membranes is considerably simpler than that of the biological membranes, which contain myriad different amphiphilic molecules, proteins, and complex carbohydrates. They therefore make good model systems for experiments on the properties and behaviour of bilayer membranes. Furthermore, pharmaceutical researchers are attempting to use artificial vesicles to encapsulate and deliver drugs to specific locations in the body. Methods of reliably creating vesicles on demand are necessary for this purpose and for research.

One typical method is extrusion; this technique will be discussed in this chapter. Experiments by the research group of Pieter Cullis have pioneered this field, creating a substantial empirical body of knowledge on extruding vesicles and the biochemical properties of these vesicles. A number of theories and hypotheses have been proposed to explain the results of these experiments, three of which are discussed in the second part of this chapter.

3.1 Vesicle Structure

The vesicles considered in this research are composed of phospholipid molecules. Phospholipids, or simply "lipids," are amphiphilic molecules; i.e., one or more regions of the molecule are composed of chemical groups that are hydrophilic (e.g., polar, ionic or zwitterionic) and other regions are composed of chemical groups that are hydrophobic (such as hydrocarbon chains). A diagram of one of the types of phospholipid molecules used in this study, 1,2-dimyristoyl-*sn*-glycero-3-phosphatidylcholine (DMPC), is shown in Fig. 3.1. As suggested by its name, this molecule contains a phosphate group as part of its headgroup. To this phosphate group is attached a positively charged choline group, $CH_2CH_2N^+(CH_3)_3$. When the molecule is immersed in water, the hydrogen atom on the phosphate group will dissociate, leaving an oxygen with a negative charge. Since the nitrogen of the choline group is already positively charged, this molecule is therefore a zwitterion for our experimental purposes. The other end of the phosphate group is attached to a glycerol backbone at the glycerol group's 3 position. To the glycerol are attached two hydrocarbon chains at the 1 and 2 positions, which form the tail of the lipid molecule. In this case, both hydrocarbon chains are the same and consist of an saturated hydrocarbon chain 14 carbon atoms long known as a myristoyl group. The molecule is synthetic; this can be inferred from the fact that both hydrocarbon chains are the same length, something which occurs infrequently in nature. (Natural phospholipids commonly have a hydrocarbon chain that is two carbon atoms longer at the 2-position than the chain at the 1-position. This gives the molecule a "flat" bottom, which may be helpful for reduction of interactions between individual layers of the bilayers.)

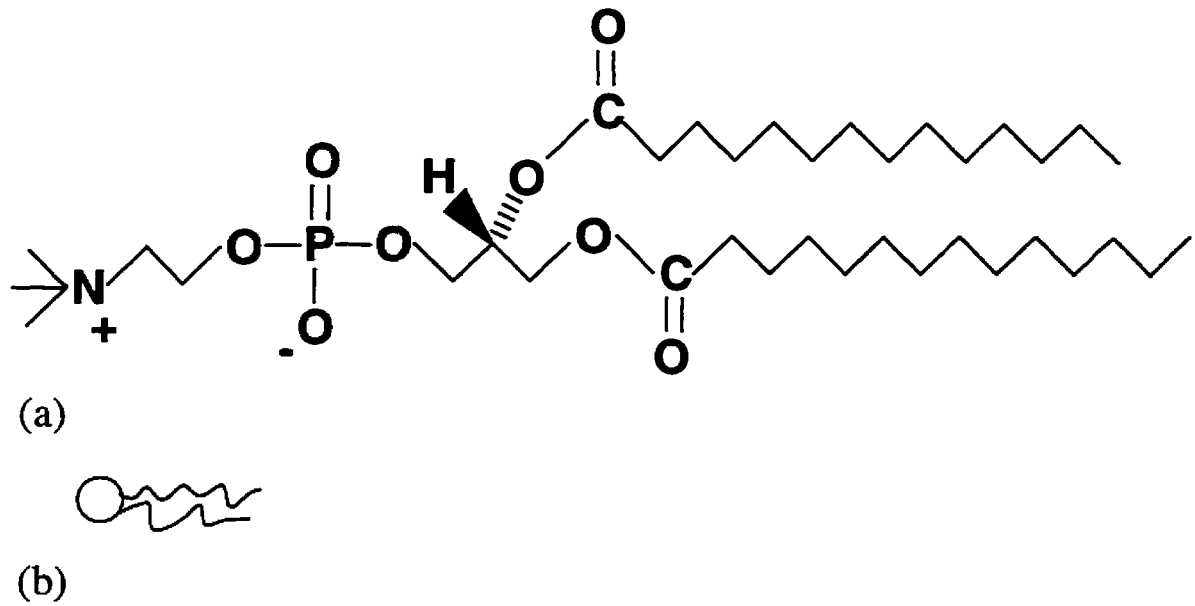

Figure 3.1: (a)Chemical structure of a DMPC molecule. (b) For simplicity, phospholipids making up larger structures will be represented by the small schematic diagram.

Vesicles form because of the hydrophobic effect. In pure water, each water molecule is hydrogen-bonded to its four closest neighbours, forming a tetrahedral network. When molecules or ions are placed in solution in water, they disrupt the molecular network of the water, reducing the possible number of arrangements of hydrogen bonds and forcing a more ordered structure on the water molecules. This decreases the entropy of the water substantially [14]. Unless there is also a gain in energy due to water-molecule/ion interactions sufficiently large to counteract the decrease in entropy, the molecules/ions will separate from the water to minimise the decrease in entropy. Ions and most polar molecules have attractive interactions with water that are stronger than the entropic cost to accomodate the ion/molecule. Such species are called *hydrophilic*, and are commonly also hygroscopic.[1] On the other hand, the interactions of most non-polar molecules with water are not strong enough to overcome the entropy barrier, and hence they have very low solubilities in water. These molecules are said to be *hydrophobic*, and their behaviour of spontaneously separating

[1]There is no hydrophilic effect, per se; it is simply an extension of the attractive interaction of ions and polar molecules with water.

themselves from water (and other polar solvents) is known as the *hydrophobic effect.* It is these two effects that cause the hydrocarbon tails of the phospholipids to spontaneously phase separate from the water, with the headgroups remaining exposed. There is an extensive literature on the subject of the hydrophobic effect; several good references are books by Israelachvili [14], Tanford [15] and Safran [16].

Once the phospholipid molecules have separated from the water, they form structures as governed by the physical shape of the molecules. Phospholipids are long and roughly cylindrical in form. Thus, they prefer to arrange themselves side-by-side in layers. Figure 3.2 shows several possible molecular shapes. The shape of the surface created depends on the form of the hydrocarbon tails and the size of the head group. A phospholipid with straight chain tails and a headgroup with area similar to the tails, shown schematically in Fig. 3.2(a), will be cylindrical in shape, and will tend to form flat layers. If the headgroup is very different in area from that of the tails, or if one or both of the tails has a kink in it due to one or more unsaturated bonds, the molecule will be roughly the shape of a cone, as seen in Figs. 3.2(b) and (c), and the layer created will be strongly curved. The layer created will be either one molecular layer thick (monolayers) or two layers thick (bilayers). Monolayers can isolate the tails by forming micelles, shown in Fig. 3.3(a), or by forming at an interface between water and air or some other material, as in Fig 3.3(b). Bilayers can form either extended planar layers, as in Fig. 3.3(c), or closed structures, called *vesicles*, shown in Fig. 3.3(d). It is possible to combine more than one type of phospholipid/amphiphile so as to change the preferred curvature or other properties of the membrane.

3.2 Membrane Properties

The topic of membrane properties is, of course, a vast one. Our discussion will be limited to the three properties of membranes that are relevant in this study: the area compression modulus K_a, the bending rigidity k_c, and the lysis tension γ_c. A fourth property, the surface shear modulus, is negligible for lipid bilayers in a fluid state. There is an excellent review article on the subject of lipid properties by Bloom, Evans and Mouritsen [20].

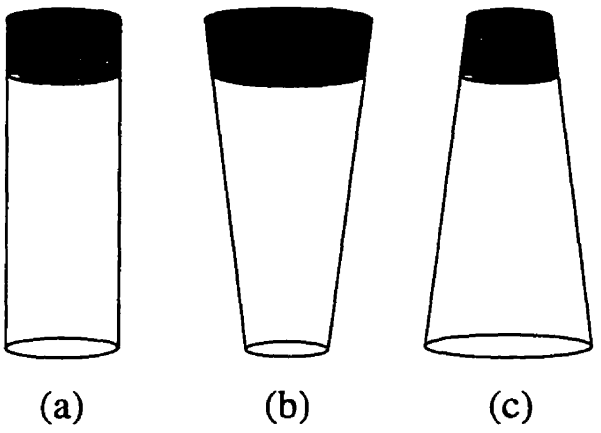

Figure 3.2: Various shapes of phospholipid molecules: (a) a cylinder, (b) a truncated cone, and (c) an inverted truncated cone. Shaded areas represent the polar head groups.

In the case of both monolayers and bilayers, the molecules are constrained to remain in the layer by the same effects that created the layer. They are, however, relatively free to move about *within* the layer by diffusion, and by flipping between layers in the case of bilayer structures. It may be noted that the layered structures of phospholipids are liquid crystalline in nature. Monolayers and bilayers are smectic liquid crystals, as they possess orientational order with respect to one another and are also ordered in the direction perpendicular to the bilayer surface. As liquid crystals, monolayers and bilayers exhibit the same phase transitions from states where the molecules are frozen in position in the layer to states where they are free to move about. (For more information on liquid crystals, see the text by de Gennes and Prost [17].)

The area compression modulus K_a gives the relationship of the fractional change in surface area, α, to the applied surface tension, γ, at constant temperature. Figure 3.4(a) illustrates the area expansion with an applied surface tension. For a vesicle in equilibrium the surface tension is zero [18, 19], but this is not the case when an external force is applied to the vesicle, such as stretching. For small changes in area, the fractional area change is

$$\alpha = \frac{\Delta A}{A} = \left(\frac{\gamma}{A}\right)\left(\frac{\partial A}{\partial \gamma}\right)_T = \frac{\gamma}{K_a} . \tag{3.1}$$

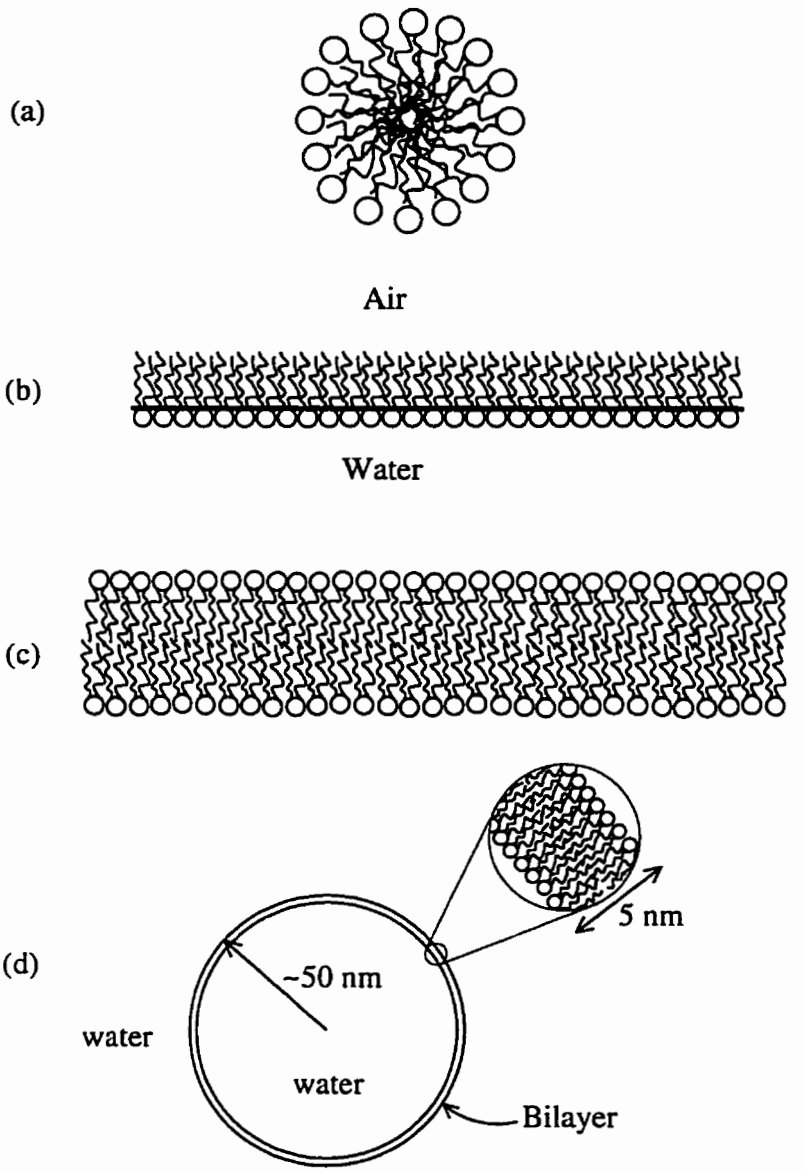

Figure 3.3: Possible structures of phospholipid molecular assemblies: (a) A micelle, (b) a monolayer at an interface between two media, in this case air and water, (c) a planar bilayer, or (d) a vesicle. All of the structures are shown in cross-section. The circular portions of the phospholipid molecules represent the headgroups. The tails are shown as curved lines.

The area compression modulus K_a, thus, has units of force per unit length. Typical values of K_a are of the order of 150 mN/m, decreasing with increasing degrees of unsaturation and increasing with the addition of cholesterol [21]. Considerable work has been done on the subjects of area compressibility moduli by Evans *et al.* [21, 22, 23, 24, 25, 26, 27] and Needham and Nunn [28].

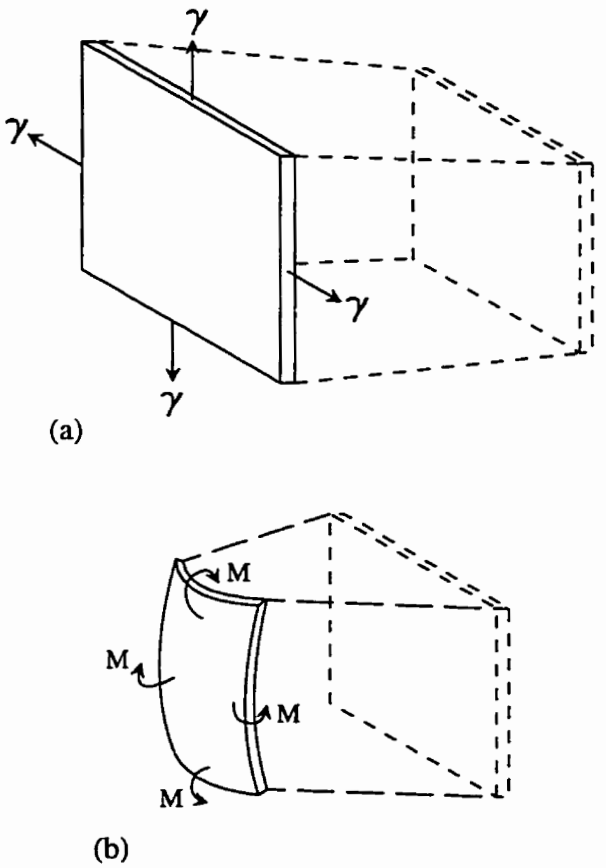

Figure 3.4: Mechanical forces on membranes. (a) Membrane expanding surface area due to surface tension γ. (b) Curvature change due to bending moment M.

In order to change the curvature of a membrane, a stress must be applied to it. The stresses associated with curvature are torques per unit length [29]. The bending rigidity (or elasticity or stiffness) k_c of a bilayer is the constant of proportionality between the bending moment M (torque per unit length) and the change in the mean

membrane curvature Δc (cf. Fig. 3.4(b))

$$M = k_c \Delta c = k_c \Delta (1/R_1 + 1/R_2) \ , \tag{3.2}$$

where R_1 and R_2 are the principal radii of curvature at a given point on the membrane surface. The bending rigidity of a bilayer is a function of the type(s) of phospholipid/amphiphile of which it is composed. Among other things, it is related to the shape of the individual molecules (cf. Fig. 3.2). Typically, the bending rigidity is on the order of 10^{-19} J. The topic of bending rigidity has been studied by Evans *et al.* [21] and Duwe *et al.* [30].

The bending rigidity may be used to find the equilibrium shape of the membrane surface given a set of fixed parameters, which may include surface area and volume. The form of the surface is determined by minimizing the free energy of the surface. Depending upon the model, the free energy may depend on the curvature of the surface, the difference in area between the inside and outside layers, the osmotic pressure difference, or some combination of these factors [31]. The free energy function proposed by Helfrich in 1973 [29] is

$$F = \frac{k_c}{2} \int dA \, (C_1 + C_2 - C_0)^2 \ . \tag{3.3}$$

Here C_0 is the"spontaneous curvature," the intrinsic curvature of the bilayer. This is a function of the composition and the environment of the two monolayers [22].

The lysis tension is the surface tension which must be applied to the bilayer to cause the surface to rupture. It is a measure of the cohesive energy of the bilayer. The lysis tension for a variety of lipids and lipid/cholesterol mixtures has been measured by Evans and Needham [25]and Evans and Rawicz [32]. These are shown in Table 5.3. (Note that these measurements have been made in the short time limit. In the long run (on the order of days), vesicles under tension will always break, no matter how low the pressure applied [33]. However, this is not of concern in these experiments as extrusion is a sufficiently quick process.) The effects of an applied osmotic pressure gradient have been studied by Mui *et al.* [34] and Ertel *et al.* [35]. It is found by the latter that the average areal expansion at rupture (which is related to the lysis tension of the membrane) is on the order of 2-3%. Both studies find values for the

lysis tension of the membrane which are consistent with studies using other methods (Needham and Nunn [28], for example).

3.3 Vesicle Production by Extrusion

A sample of vesicles can be prepared simply by mixing phospholipid(s) in powder form into water. The lipid molecules will spontaneously form large, multilamellar vesicles. The utility of the vesicles created this way is limited. It is difficult to control the concentrations, pH and other relevant parameters across these internal bilayers, since there is no direct access to them, and the number of layers contained within the multilamellar vesicles is generally unknown. The distribution of sizes of these vesicles is also extremely broad with the mean radius normally being several microns. In order for the vesicles to be useful for research and pharmaceutical applications, it is necessary to make them unilamellar. There are several methods of doing this including dialysis [36, 37, 38], dilution from organic solvents [39, 40], sonication [41], and extrusion under pressure [1, 42, 43]. The last of these methods is the focus of this thesis. Extrusion has an advantage over the other methods in that it is a purely physical process, whereas the methods of dialysis and organic solvent dilution involve contaminating the sample with detergents or organic solvents. While these contaminants, especially the detergents, are supposedly completely removed by the dialysis process, statistical mechanics tells us that there will always be a certain amount of detergent left in the sample unless we are willing to wait for an infinite period of time. Sonication does not use any contaminants, but it is difficult to control the size of sonicated vesicles, and the resulting vesicles are highly stressed and unstable to coalescing with other vesicles.

The process of extruding vesicles is quite simple: a volume of fluid containing multilamellar vesicles as described above is placed in a sealed chamber. This sealed chamber has attached to it either a high pressure gas inlet and release valve or a syringe-driven piston [2], and an exit path which is blocked by a porous filter membrane consisting of long and narrow cylindrical pores. A schematic diagram of the

extruder used in this study is shown in Fig. 3.5. A volume of solution containing suspended multilamellar vesicles is placed in the extruder using a syringe. The chamber and sample are then allowed to equilibrate at the desired temperature. (This can be significant for lipids with a crystal/liquid crystalline transition temperature near the temperature at which the extrusion is performed [43].) When the gas inlet is opened or the piston is depressed, the pressure applied to the top of the fluid forces the suspension through. The procedure is repeated until the vesicles reach the desired size and number of lamellae or until there ceases to be any improvement in the vesicles' characteristics.

Early characterization by electron microscopy (EM) [1] of vesicles made by extrusion showed that vesicles extruded through 100 nm pores had average vesicle radii of 70 nm with standard deviations of $\sim$ 20 nm. Multiple passes through the extrusion device were shown to reduce the multilamellarity of the vesicles and decrease the average size; after approximately five passes through the extrusion apparatus, the vesicles appeared to reach their final state. The population was unimodally distributed about the mean in a roughly gaussian manner. If the pores used were small enough ($<$ 200 nm in diameter), the vesicles were almost exclusively unilamellar [1].

Further studies investigated vesicles resulting from extrusion through different pore sizes [42] and from extrusion of different lipids at various temperatures [43]. Characterization by EM and DLS showed that, while extrusion through 100 nm pores resulted in approximately 100 nm vesicles, extrusion through larger pores generally yielded vesicles smaller than the pore size and extrusion through smaller pores yielded vesicles larger than the pore size. Results for different lipids indicated that there might be some lipid dependence to the final vesicle size. Extrusion was found to be unsuccessful below the gel-fluid transition temperature; this was attributed to decreased fluidity of the membrane below the transition temperature. Later studies [44] investigated the effect of extrusion pressure and lipid concentration on vesicle size over limited ranges of pressure and concentration. While no effect on size due to concentration was observed, the size of the vesicles was found to decrease slightly with increasing extrusion pressures.

All of this data is purely empirical. There is no real understanding of how the

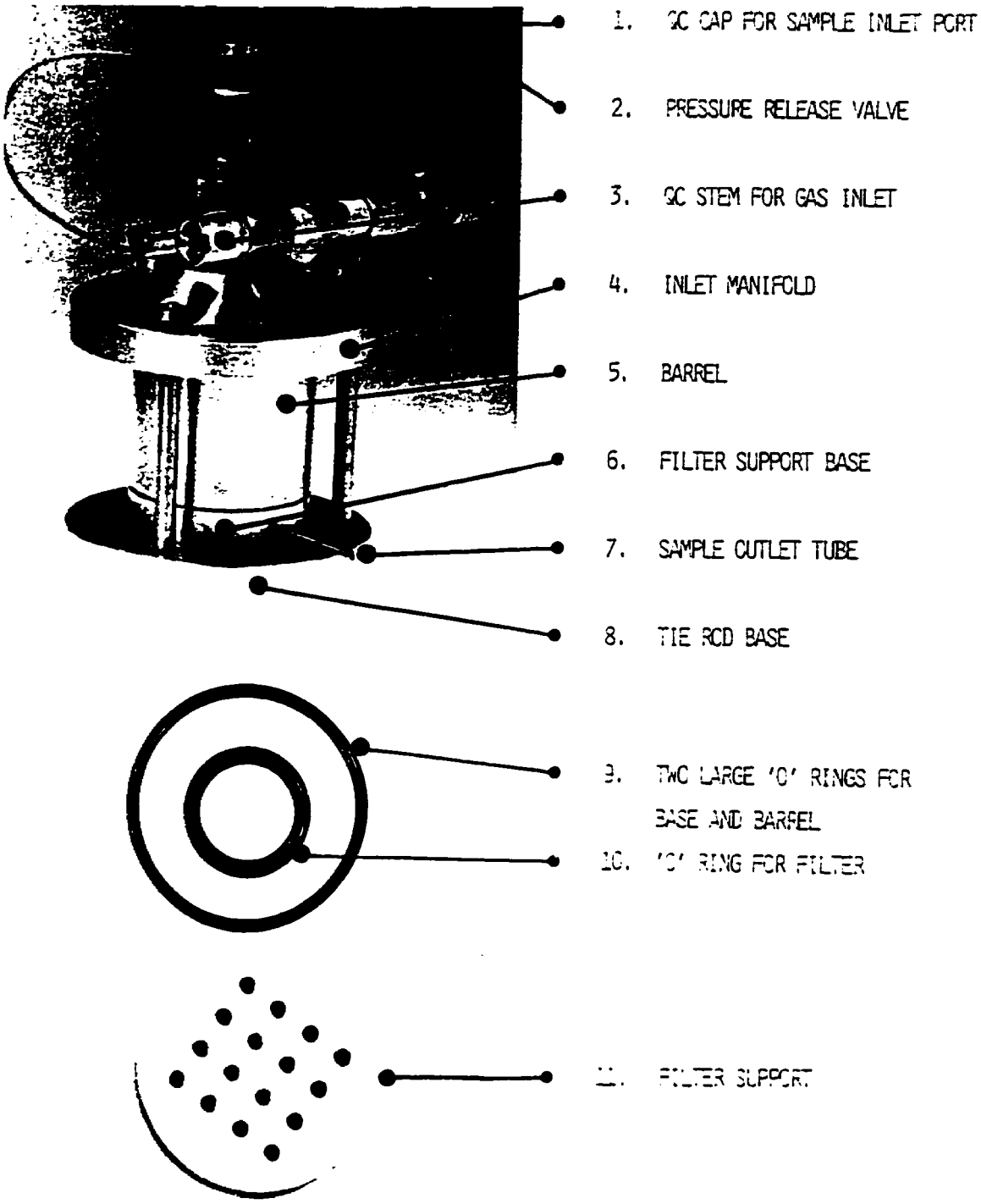

Figure 3.5: A diagram of the Extruder™ labelling the major components.

vesicles are created by this procedure. The problem is a challenging one, as the size of the object in question, ~100 nm, is a difficult range to probe. By its very nature, the system is a dynamic one and not steady-state. Most of the theoretical descriptions of vesicles assume that the system is at or close to equilibrium or that the system is exhibiting steady-state behaviour and neglect possible membrane rupture. The fact that the vesicles are suspended in water that is itself flowing makes this a problem of fluid mechanics. Essentially, the problem is this: how and in what order does a giant, multilamellar vesicle enter the pore, break up, and reform itself into a number of small, unilamellar vesicles of the same approximate size as the pore?

3.4 Theories of Extrusion Mechanisms

There are three different theoretical pictures of the behaviour of vesicles in pores. The first, proposed by Clerc and Thompson [3] in 1994, treats the formation of vesicles as a variation of the Rayleigh instability. The second, from Gompper and Kroll [4], uses a Monte Carlo algorithm to simulate a vesicle being deflated and pushed through a pore by a driving force. Bruinsma [5] looks at the problem as one of capillary flow, with the vesicles decreasing the permeability of the filter membrane.

3.4.1 Capillary Flow

Before dealing with the problem of suspended vesicles in a viscous fluid undergoing flow, let us consider a homogeneous viscous fluid flowing in a pipe of circular cross-section. This is of course a particularly relevant question, since the suspensions that are being extruded are still mostly water. The behaviour of pure water flowing through the filters will taken as baseline by which to judge the vesicle extrusion experiments.

Assuming that the flow through the pore is laminar, it can be shown the rate of volume flow of fluid q through a cylindrical channel or pore is given by [45]

$$q = \frac{\pi R_p^4}{8\eta}\left(\frac{\Delta P}{L}\right), \tag{3.4}$$

where R_p is the radius of the channel, η is the viscosity of the fluid, L is the length of the channel, and ΔP is the pressure difference between the ends of the channel. The

factor of $\pi R_p^4/8$ is due to the assumption that the channel is circular in cross-section, and will vary for differing geometries. To relate q to the observed flowrate Q, we assume that the pores all have the same radius[2] and multiply q by the number of pores per unit area N and the available area A, such that $Q = NAq$. Equation 3.4, expressed differently, is known as Darcy's law:

$$\eta Q = K\left(\frac{\Delta P}{\Delta L}\right) , \tag{3.5}$$

where K is the permeability of the filter. It is interesting to note that the product of the viscosity and the flowrate ηQ (hereafter referred to as the viscosity-corrected flowrate) is independent of temperature. Measurement of the viscosity-corrected flowrate as a function of pressure or pore length will then give the value of the filter permeability K.

The Reynolds' number $\mathcal{R}$ for this system is 0.045 at most, very far from the onset of turbulence ($\mathcal{R} \sim 2000$). This absence of turbulence is due primarily to the narrowness of the pores.[3]

3.4.2 Vesicle Flow Through Pores

To explain the formation of vesicles by extrusion, Clerc and Thompson [3] have proposed the following picture. The flow of water through the pores sucks multilamellar vesicles into the pores. The shear field due to the velocity profile creates concentric cylindrical lamellae of lipid bilayers. Because the shear field is pulling on them, the lamellae are under tension. When the cylinders reach the end of the pores, they break up into smaller structures. Using a result from emulsion theory [46] that cylindrical structures which are not somehow constrained to this shape are unstable to perturbations with wavelength $\lambda > 2\pi R$, where R is the radius of the cylinder, they estimate the area of the bilayer that will be broken off by the instability. By equating this area

[2]This is not actually true, as will be discussed later.

[3]This assumption is certainly valid in our experiments. As will be described more fully in Ch. 4, the highest observed flowrate Q was 3.55 mℓ/s, which corresponds to a mean flow velocity v of 0.29 m/s for a cylindrical pore 50 nm in radius. The maximum velocity in the centre of the channel is twice the mean velocity. The Reynolds' number for flow in a pipe is defined as $\mathcal{R} = v_{max} R_p \rho/\eta$ [45], ρ being the density of the fluid, in this case water.

with the area of a spherical vesicle, they predict that the final spherical vesicle should have a radius 1.77 times the radius of the cylindrical lamella from which it originated. The model does not include a way of determining the radius of the cylindrical lamellae directly, but it may be possible to estimate this from the size of observed vesicles.

The origins of the emulsion theory result lie in the "Rayleigh instability" [47] which predicts the breakup of a cylinder of fluid into droplets. The most common example of this can be seen in a stream of water from a faucet, which, while initially cylindrical, invariably breaks up into droplets. This is illustrated in Fig. 3.6. Rayleigh treats this system as a cylinder with a small cylindrically symmetrical perturbation on its surface. The only force acting on the system is the surface tension, which acts to minimise the surface area. This is constrained by the requirement that the total volume of fluid in the cylinder must be conserved. From this, it can be readily shown that perturbation modes with wavelengths greater than $2\pi R$ are unstable. He then goes on to show that the fast-growing mode is that with $\lambda = 4.508 \cdot 2R$.

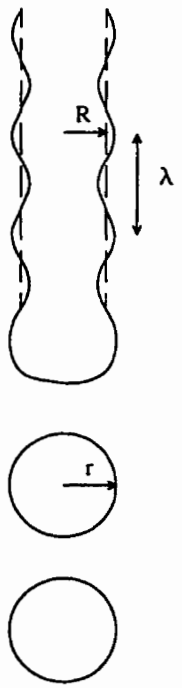

Figure 3.6: The Rayleigh instability. A column of fluid of mean radius R undergoing a perturbation of wavelength λ is unstable, and will break up into droplets of radius r.

There are a couple of possible problems with the application of Rayleigh's results to the problem of extruded vesicles. The first is the fact that vesicles have the requirement that area be conserved instead of volume. Secondly, the function that should be minimised is the bending free energy, such as the Helfrich free energy in Eq. 3.3. The question of whether or not this leads to the same instability has been examined for a similar problem by Bar-Ziv and Moses [48]. Their analytical technique follows that of Rayleigh, and leads to a stability phase diagram with the reduced initial tube radius x and the reduced ratio of the surface tension to the bending modulus s. For small values of s, say $s < 2$ for $x < 0.75$, the cylindrical tube is stable. The cylinder is stable at increasing values of s for $0.75 < x < 1$. For s between 2 and 6, the cylinder is unstable to an undulating peristaltic mode. Above $s \sim 6$, the peristaltic mode is unstable to "pearling." In this mode, the cylinder collapses to a chain of isolated spheres connected by thin ($\sim$ 200 nm) tubes. This instability is essentially the Rayleigh instability, as large s implies that the surface tension is dominating the bending modulus. A rough estimate of s with our experimental parameters gives a value of 175, so that the Rayleigh instability dominates. It is conceiveable that these spheres might be pulled apart by external shearing during extrusion, although this did not occur in Ref. [48]. Questions about the applicability of these results to extrusion are due to the length scales of the experiments in Ref. [48]. Typically, the initial radius of the cylindrical vesicles was 1.5 μm and the "thin" tubes were 200 nm in radius, which are 30 and 4 times respectively the approximate initial radius of our hypothetical cylinders. At such small scales, the effects of bending the membrane are much more pronounced, so that we are not sure where we are in the phase diagram, or even if the phase diagram is still applicable.

There is also the question of the location of the breakup of the cylindrical lamellae. Clerc and Thompson suggest that the breakup should occur just after the lamellae have exited the pore, and the shear-induced tension has dropped to zero. However, recent results [5, 31] suggest that the cylindrical form may be unstable inside the pore given a great enough shearing force.

In contrast to Clerc and Thompson, Gompper and Kroll [4] have taken the approach of simulating the passage of vesicles through pores using a Monte Carlo algorithm. A linear driving potential is applied to force the vesicles through the pore. This is equivalent to a constant electric field, but not necessarily to a pressure gradient [49]. An applied pressure can result in the two following situations: 1) If the pore is not blocked, the suspending fluid will be flowing, with a spatially varying velocity field. This results in a complex, non-uniform pressure field, which is definitely not linear. 2) A pore blocked by a stationary vesicle will prevent fluid flow. In the absence of flow, the pressure is the same everywhere in the fluid. All of the pressure drop occurs over the vesicle in a discontinuous way.

In spite of the fact that the situation examined is not the same as that under consideration here, the model does give some insights. The most significant conclusion is the prediction of the existence of a minimum applied field f^* below which it is not possible to push the vesicles through the pores. Above this threshold, the vesicles are sucked into the pore. According to this model, the threshold field is proportional to the bending rigidity of the bilayer, i.e., $f^* \propto k_c$. The mobility of the vesicles, the velocity of the vesicle's centre of mass divided by the applied force, scales with k_c as a power law with an exponent of 1.2 ± 0.2. By analogy, it is not unreasonable to think that there would be a minimum pressure P_{min} associated with k_c required to cause the vesicles to go through the pores. It is important to bear in mind that this minimum pressure exists in the short-time limit only, since the vesicle will always break eventually, as previously stated. No provision was made in the model for the possibility of rupturing the vesicle, which we believe is a critical factor in any theory concerning vesicle extrusion. Unfortunately, the model used for the simulations does not lend itself easily to breaking up the surface into several smaller surfaces. Instead, the volume of the vesicle was allowed to vary freely, permitting easy changes in topology.

An alternate viewpoint is provided in a recent paper by Bruinsma [5]. This study assumes that insertion of the vesicle into the pore has already been accomplished and proceeds to investigate the fluid mechanics surrounding the flow of the vesicle through the pore. In doing this, it has drawn heavily on research on the flow of bubbles in tubes and red blood cells in capillaries [50, 51, 52]. The paper looks at steady-state

flow of a vesicle in a capillary or cylindrical pore, taking as its starting point the capillary flow described above. The vesicle begins with the shape of a spherocylinder. The shape of the vesicle can change as volume is forced out of it. Bruinsma then proceeds to derive the Navier-Stokes equations for the system. The main prediction is that above a certain pressure, set by the osmotic pressure in the vesicle, the flow velocity through the pore is independent of the bending energy of the bilayer, and that the only effect of the vesicles is to cause a decrease in the permeability. This is a significantly different result from that of Ref. [4]. Darcy's law is then

$$\eta Q = \frac{NA\pi R_p^4}{\left(8 + 0.233 \times (nL^*)\,\frac{L^{*2}}{R_p^2}\right)}\left(\frac{\Delta P}{L}\right) , \tag{3.6}$$

where n is the number of vesicles per unit length in the pore and L^* is the length of the spherocylindrical vesicle in the pore (cf. Eq. 3.5). A schematic diagram of a vesicle in a pore is shown in Fig. 3.7.

The permeability K, hereafter referred to as K_{eff}, is obviously now

$$K_{eff} = \frac{NA\pi R_p^4}{\left(8 + 0.233 \times (nL^*)\,\frac{L^{*2}}{R_p^2}\right)} . \tag{3.7}$$

The only characteristics of the lipid mixture that the effective permeability depends on is the number of vesicles in the pore and the size of those vesicles. This contrasts sharply with the model of Gompper and Kroll, in which the parameters of the model were dependent on the bending modulus of the bilayer. Derivation of Eq. 3.7 involves consideration of the thickness of the lubrication layer h^* between the vesicle and the wall of the pore and the assumptions that $h^* \ll R_p$ and that the interaction potential of the bilayer with the pore wall is negligible at this distance. The thickness of the lubrication layer is a function of the flow velocity V in the pore and is given by

$$h^*(V) \;=\; 2.05 \times R_p \left(\frac{\eta\, V}{\gamma}\right)^{2/3} , \tag{3.8}$$

where γ is the surface tension in the lipid bilayer. As V increases, and h^* increases, the radius of the vesicle in the pore will decrease. Physically, the radius cannot decrease

indefinitely so some limit on the thickness of the lubrication layer should be imposed. This has not been included in the model. The surface tension quoted here is that of

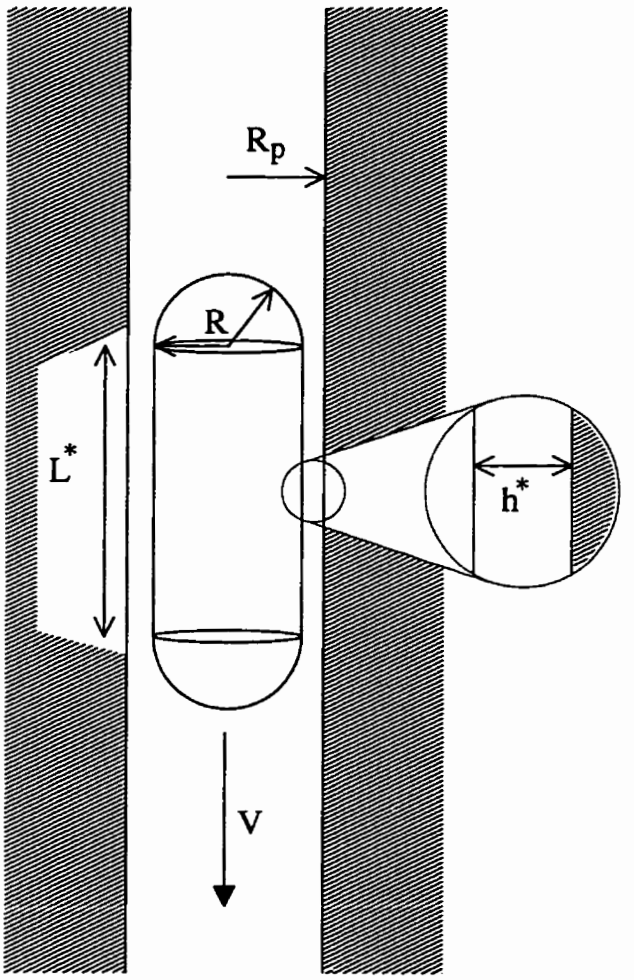

Figure 3.7: Schematic diagram of a vesicle in a pore of radius R_p. The vesicle is a spherocylinder of length L^* and endcap radius R. The vesicle moves through the pore at velocity V and is separated from the pore wall by a lubrication layer of thickness h^*.

the front endcap of the vesicle, the hemispherical region of the bilayer on the front of the vesicle. This portion of the membrane has the highest surface tension, decreasing along the length of the cylindrical section of the vesicle until it reaches zero tension at the rear endcap. (As it has the highest tension, the front endcap is expected to be the place where any vesicle rupture will take place.) The tension is predicted to

increase linearly with flow velocity V and therefore with volume flowrate[4]

$$\gamma = 0.1165 \times \left(\frac{L^*}{R}\right)^3 \eta V. \tag{3.9}$$

The surface tension cannot increase indefinitely, of course. It is reasonable to think that the vesicle will rupture when the velocity V is great enough to cause the surface tension to exceed the lysis tension for the vesicle.

Below an osmotically determined threshold pressure, the permeability is no longer independent of flow velocity. Darcy's law ceases to be obeyed, and the flowrate is not linear in the pressure. The flowrate is predicted to reach zero at zero applied pressure head, i.e. no minimum pressure is expected.

In addition to the assumption of steady-state flow, which is dubious at best, Bruinsma has assumed that the boundary layer thickness h^* is much less than the radius of the pore R. Note that h^* is a function of the flow velocity through the pore and of the surface tension on the vesicle. While this may be true for red blood cells flowing in blood vessels, it is not at all clear that this is so for vesicles being extruded through 100 nm diameter pores. It remains to be determined from experiment whether or not this assumption is valid.

It is important to note that the situations and results described in the models of Bruinsma and of Gompper and Kroll are not the same as extrusion of vesicles through small pores. That is, they are not so much wrong as they are inapplicable to the problem. Nevertheless, both studies capture parts of the problem and present some interesting ideas.

[4]Equation 3.9 may seem to be inconsistent with Eq. 3.8. This is not the case because Eq. 3.9 was derived using Eq. 3.8.

Chapter 4

Experiment and Results

4.1 Materials and Methods

The phospholipids used were 1,2-dimyristoyl-*sn*-glycero-3-phosphatidylcholine (or DMPC), 1-stearoyl-2-oleoyl-*sn*-glycero-3-phosphatidylcholine (SOPC), and 1,2-di-oleoyl-*sn*-glycero-3-phosphatidylcholine (DOPC) in powder form. These were purchased from Avanti Polar Lipids, Inc. of Alabaster, Alabama. These lipids were chosen because of the ready availability of data on their physical properties. The headgroup type, phosphatidylcholine, was kept the same so that the only variation in vesicle properties would be due to the effects of the lipid tails. The degree of saturation and lipid chain length varied over all of the lipid types. The myristoyl chains of DMPC are 14 carbon atoms in length and are saturated, that is, there are no double bonds. SOPC has a saturated stearoyl chain of 18 carbons and an unsaturated oleoyl chain of 18 carbons with one double bond. The double bond is a *cis* bond [53], making the molecule somewhat unstable at room temperature. DOPC has two oleoyl chains. The effects of increasing degree of unsaturation are to lower the crystal-liquid crystalline phase transition temperature and to decrease the bending rigidity and area compressibility moduli.

4.1.1 Preparation of phospholipid vesicles

For each sample, a single variety of phospholipid was hydrated using purified water from a Milli-Q Plus water purification system (Millipore, Bedford, MA), in ratios of 1-2.5 mg of phospholipid per mℓ of water. The Milli-Q Plus filtration system ensured that the concentration of contaminants in the vesicle solution was negligible. The presence of unknown chemical contaminants may lead to undesirable and uncontrolled chemical and osmotic effects in the vesicles, while large particulate contamination will interfere with the light scattering experiments. The mixtures of water and phospholipid were taken through a freeze-thaw procedure five times. This involved freezing the solution by immersing the flask containing the sample in liquid nitrogen, thawing the flask in 50° C water and vortexing thoroughly. This has been found to help break up the multilamellar vesicles and promote the mixing of the enclosed contents with the exterior solution [54]. Normally, a 25 mℓ Pyrex volumetric flask, containing less than 20 mℓ of solution is used for the freeze-thaw process. This is the largest glass container that can withstand the severe stresses due to the freeze-thaw process and (more importantly) to the expansion of the water upon freezing.

After the freeze-thaw-vortex process, the vesicle suspension was cleaned and regularized by extruding it once through two polycarbonate membrane filters (Osmonics-Poretics Inc., Livermore, CA) with pore diameter 400 nm. This process, which we call pre-extrusion, was found to improve the repeatability of the light scattering experiments and measurements of the extrusion flowrate. This is the primary variation of our procedure from the one described by Hope *et al.* [1].

Prior to extrusion through the final filter size, the pre-extruded vesicle suspension was diluted with purified water to a concentration of 1 mg of phospholipid per mℓ of water. Note that this procedure of diluting the vesicles to the desired concentration just prior to extrusion should only be used if there is no harm in mixing the contents of the vesicles with the exterior solution. The pre-extruded vesicle suspension was then extruded a minimum of 10 times through two polycarbonate membranes with a nominal pore diameter of 100 nm, using an Extruder (Lipex Biomembranes, Vancouver, BC) by applying a pressure gradient. The pressure gradient across the membranes

was created using pre-purified, compressed N_2 gas. For each phospholipid, a series of extrusions was made at a range of pressures at a single temperature. The DMPC suspensions were extruded at pressures ranging from 30 psi to 300 psi for 25°C, 30°C and 40°C. The SOPC and DOPC suspensions were extruded at 30°C, with pressures ranging from 300 psi down to 65 psi for DOPC and 50 psi for SOPC.

The vesicle suspension was re-extruded a minimum of ten times or until the macroscopic bulk flowrate became constant. The macroscopic bulk flowrate of the extruded suspension was measured either with a stopwatch and a graduated cylinder, or by observing a video recording of the flow into a graduated cylinder. The purpose of this was to measure the final flowrate and to determine whether or not the flowrate was correlated with the final size of the vesicles.

The polycarbonate membranes (Osmonics batch no. AE84AH11C007) used in these experiments nominally consist of cylindrical pores with a diameter of 100 nm. However, this is not the average pore size; discussions with the manufacturer reveal that the membranes should have no pore larger than 100 nm. However, the manufacturer's electron microscope (EM) measurements of characteristic membranes from this batch show that there are pores distributed between 108 and 88 nm, with a mean diameter of 93 nm and a standard deviation of 6 nm. This batch has a fairly narrow distribution. Typically the distribution is somewhat broader. Independent EM observations [55] do not seem to corroborate these results, with some pores being twice the manufacturer's stated maximum diameter. Furthermore, the pores are not perfectly cylindrical but are slightly barrel-shaped, being on the order of 10% greater in diameter in the center of the membrane than at the edges. This is due to the etching process used in the manufacture of the membrane, and is intentional on the part of the manufacturer, as it supposedly increases the rate of flow through the filters without increasing the size of the entry to the pore.

4.2 Light Scattering Apparatus

The apparatus used for the DLS and SLS experiments was an ALV DLS/SLS-5000 spectrometer/goniometer manufactured by ALV-Laser GmbH of Langen, Germany. A

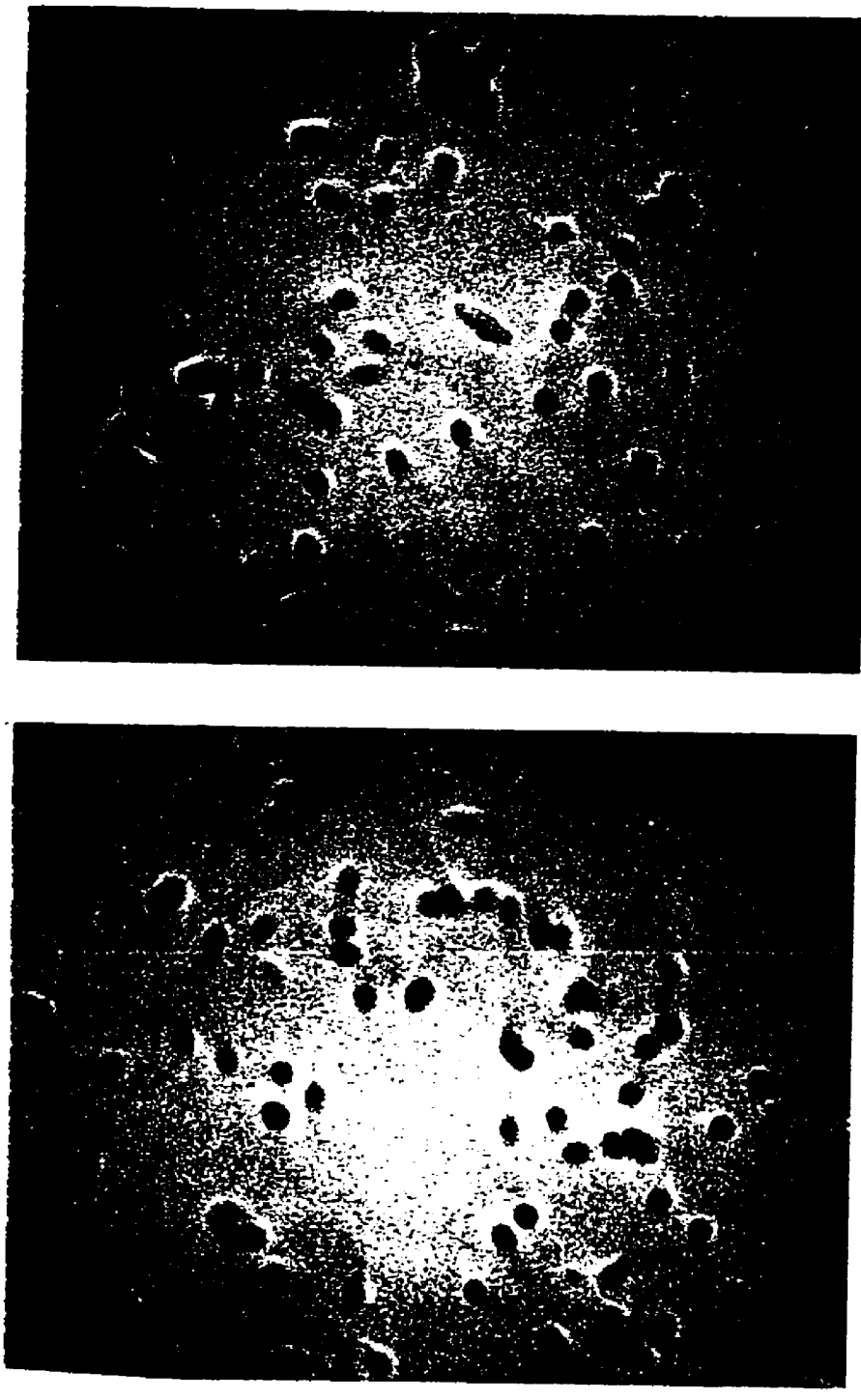

Figure 4.1: Electron microscope photographs of two different sections of the surface of a polycarbonate filter membranes from the same batch as was used in the experiments. The magnification of the photo is 22000×.

schematic view of the physical arrangement is shown in Fig. 4.2. The ALV apparatus consists of laser alignment optics, a temperature-controlled scattering chamber, a set of detection optics connected to a photomultiplier tube (PMT) and a correlator. The motorised goniometer is computer controlled and mounts the photomultiplier tube and accompanying optics to permit measurements to be made at a variety of scattering angles. All of the optics are enclosed to keep out stray light. A Spectra-Physics Model 127 35 mW helium-neon laser of wavelength λ= 632.8 nm is used as the light source. The apparatus and laser are mounted on a Melles-Griot optical table to isolate them from external vibration and noise. A more complete description of this apparatus is given by Lau [56].

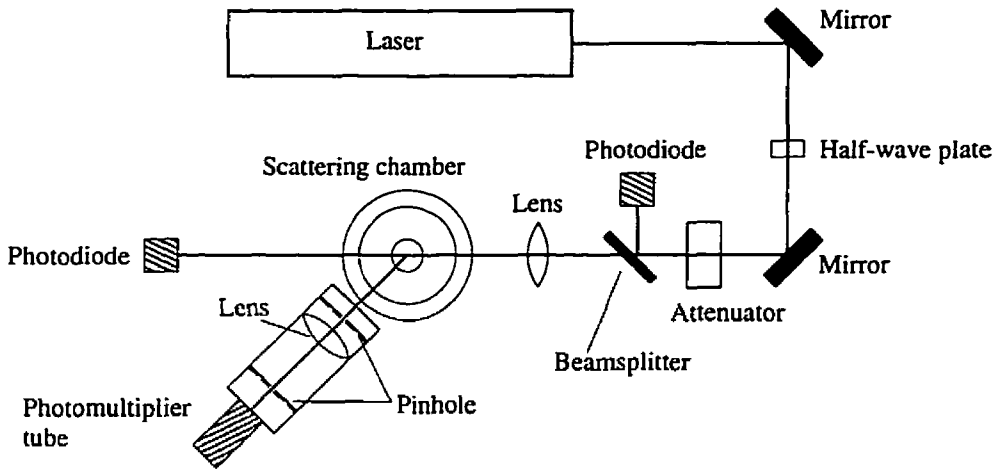

Figure 4.2: Light scattering apparatus.

The scattering chamber itself is a cylindrical quartz vat which is filled with fluid. For these experiments that fluid was toluene. Samples were contained in cylindrical glass ampules which were suspended in the toluene from above. Toluene was chosen to minimise the difference in refractive index between it, the ampule, and the quartz vat. The sample temperature was regulated by controlling the toluene temperature. The toluene bath temperature was controlled by means of thermally coupling it to a Neslab RTE-100 Refrigeration Bath/Circulator, which has a temperature range from -15°C to +130°C with a stability of ±0.01°C. The sample temperature is taken to be the same as that of the toluene.

4.3 Vesicle Characterisation by DLS and SLS

Prior to size and size-distribution analysis of the sample by DLS and SLS, the vesicle suspension was diluted in Milli-Q water to approximately 0.1 mg of phospholipid per mℓ of fluid and placed in a glass vial. This was to ensure that the number density of vesicles is low enough so that the inter-vesicle interactions are minimised and so that we are in the single-scattering regime. The sample, contained in a 10 mℓ cylindrical glass vial, was placed in the toluene bath and allowed to equilibrate thermally for one hour so that any convection currents subside. The toluene bath was maintained at the temperature at which the vesicles were extruded, in order to minimise thermal expansion and/or contraction of the vesicles. Light from the He-Ne laser passed through the sample and light scattered by the sample was detected at angles of 60°, 90°, and 120° from the transmitted beam for DLS measurements and at 23 angles from 16° to 150° for SLS measurements by the photomultiplier tube (model 9130, EMI Hayes, England).

Using the techniques described in Chapter 2, the non-linear least square fitting routine nllsq was used to fit the field-field correlation function $g^{(1)}(\tau)$, and hence $g^{(2)}(\tau)$, to the DLS data to obtain $\overline{\Gamma}$ and μ. The weights for the data points were calculated internally by the ALV-5000 correlator by a complex algorithm related to the number of observed counts for a given correlation time τ. The mean and variance of the hydrodynamic radius R_h were calculated from the fitted quantities $\overline{\Gamma}$ and μ using the Stokes-Einstein relation.

The DLS measurements reported here were taken at 90°, where the effects of reflection are minimised, since light that reflects off the interior of the vat and then scatters off a vesicle or vice versa always has a scattering angle of 90°. At any other scattering angle θ, the reflected scattered light will have a scattering angle of $180° - \theta$, with the result that two differing decay rates may be present in the signal. This has the effect of broadening the apparent decay rate distribution width. Conveniently, the effects of polydispersity are also small at this angle, due to a coincidence of vesicle size and scattering vector [56]. The hydrodynamic radius was measured five times at 90° for all samples. These five radii were averaged to find a mean radius $\overline{R}_h$. The

standard deviation of this average was used to get an estimate of the repeatability of the measurement and was taken as an estimate of the uncertainty in $\overline{R}_h$. The variances of the five measurements were also averaged to find a mean variance $\overline{\mu}$. The standard deviation of the distribution σ was calculated from $\overline{\mu}$.

The radius of the vesicles was also measured by analysis of the static light scattering data. The model function using the form factors for hollow spheres with a finite thickness of 4.2 nm described in Chapter 2 and Appendix B was fit to the data using the nnlsq routine. This thickness was chosen to agree with measurements of typical lipid bilayers. Typical SLS data and a fit to this data are shown in Fig. 4.3. This fit had two parameters, the outer radius R_o and a constant arbitrary intensity factor. The sizes of vesicles obtained by fitting the SLS data were consistent with those obtained by DLS experiments, hence static light scattering was used primarily to confirm the results obtained by the DLS experiments. Zero polydispersity was assumed in these fits, as non-zero polydispersities resulted in worse fits, for reasons which are not yet understood.

4.4 Results

Figures 4.4 through 4.6 show the radius, the relative standard deviation of the vesicle size distribution, and the flowrate for a typical extrusion experiment, respectively. In this case, the DMPC solution was extruded through 100 nm polycarbonate membrane filters at 200 psi and 30° C. As seen in Fig. 4.4, the radius decreases rapidly to about 120% of the pore radius in four extrusions. The radius relative to the pore radius is shown on the right hand axis. After four extrusions, the size continues to decrease, but more slowly, so that by the tenth extrusion the vesicle radius is 12% larger than the pore radius. Similarly, the relative standard deviation $\sigma/\overline{R}_h$ (Fig. 4.5) decreases quickly with the first three extrusions, and then levels off to a roughly constant level. As apparent from Fig. 4.6, there is no discernible trend in the flowrate over the series of extrusions. This is typical of extrusions made at pressures $\geq$ 100 psi. At lower applied pressures, a larger number of extrusions are required to reach a constant flowrate.

Similar extrusions were made of different lipid solutions at different temperatures and over a range of pressures. Final measurements of R_h and $\sigma_{R_h}/\overline{R}_h$ for DMPC extruded at 25° C, 30° C and 40° C are shown in Fig. 4.7 and Fig. 4.8. For a given extrusion pressure, there is little difference in the mean radius R_h and the relative standard deviation $\sigma_{R_h}/\overline{R}_h$ between different temperatures. In general, the size of the vesicles decreases as the extrusion pressure increases. Surprisingly, there is no corresponding decrease in the relative standard deviation. It is not possible to extrude significant numbers of DMPC vesicles at or below approximately 30 psi. At pressures at or below 30 psi, some fluid does pass through the polycarbonate filter membranes, but at an exceedingly low flowrate; however, the fluid that is extruded does not contain sufficient vesicles upon which to perform light scattering experiments. Thus, there is a minimum pressure to extrude vesicles through narrow pores, hereafter referred to as P_{min}. This definition assumes that a significant, i.e., measurable volume of fluid is extruded in a period of time less than six hours. This seems reasonable since producing vesicles requires at least ten extrusions would require over two days at this rate! Furthermore, at this sort of time length we may be entering a quasi-equilibrium regime where other factors such as vesicle deflation may become important.

The number of extrusions required to reach a constant flowrate at a given extrusion pressure is shown in Fig. 4.9. The uncertainties in the number of extrusions required are due to imprecisions in the method of flowrate determination. We have associated a constant flowrate from one extrusion to the next with reaching a final size distribution. Beyond this point, the flowrate does not increase further, implying that the sizes of the vesicles are not changing. The number of extrusions to reach a constant flowrate was generally greater at higher temperature, especially at low pressures. At high pressures, the number of extrusions required eventually reached one at all temperatures.

The DOPC and SOPC solutions behaved similarly to the DMPC solution. The results for extrusions done at a range of pressures are shown in Fig. 4.10 through Fig. 4.12. As seen in Fig. 4.10, at high pressure, the DOPC and SOPC vesicles are slightly larger than the DMPC vesicles extruded at the same pressure, but all samples show a decrease in radius with extrusion pressure. The minimum pressure required for extrusion varied significantly between lipids. The minimum pressures for which

DOPC and SOPC were extruded were approximately 65 psi and 55 psi, respectively. Figure 4.11 shows that there is no change in the relative standard deviation as a function of pressure for any of the phospholipids. The number of extrusions required to reach a constant flowrate was greater for DOPC and SOPC than for DMPC in the intermediate pressure range, as shown in Figure 4.12. At 300 psi, the number of extrusions required was the same for all of the lipids. The number of extrusions required became more disparate as the vesicles of each type of phospholipid approached their minimum pressures.

The macroscopic bulk flowrate as a function of extrusion pressure is shown for various lipids and temperatures in Fig. 4.13. The flowrate of water at 30° C is plotted for comparison. Except in the region near the minimum pressure, the flowrate of the vesicle suspension depends more strongly on the temperature, shown in Fig. 4.13(a), than on the type of phospholipid, as shown in Fig. 4.13(b). Above 100 psi, the flowrate is independent of the lipid involved.

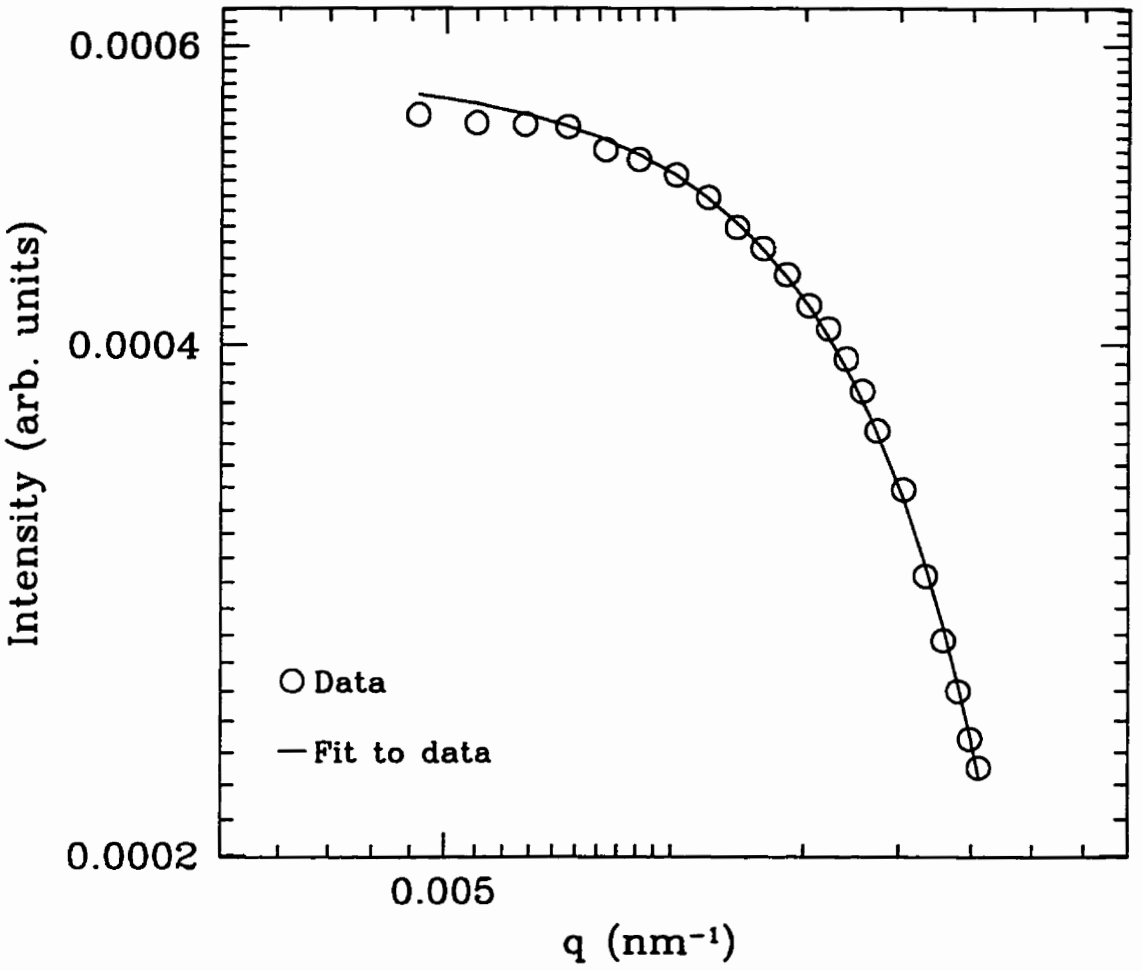

Figure 4.3: Static light scattering data and fits to the data for a typical sample of vesicles. The sample in this case is composed of SOPC vesicles extruded at 100 psi and 30°C. The lipid concentration is 1 mg/mℓ. The fit to the data yields a radius of 65.1 nm $\pm$ 0.268 nm.

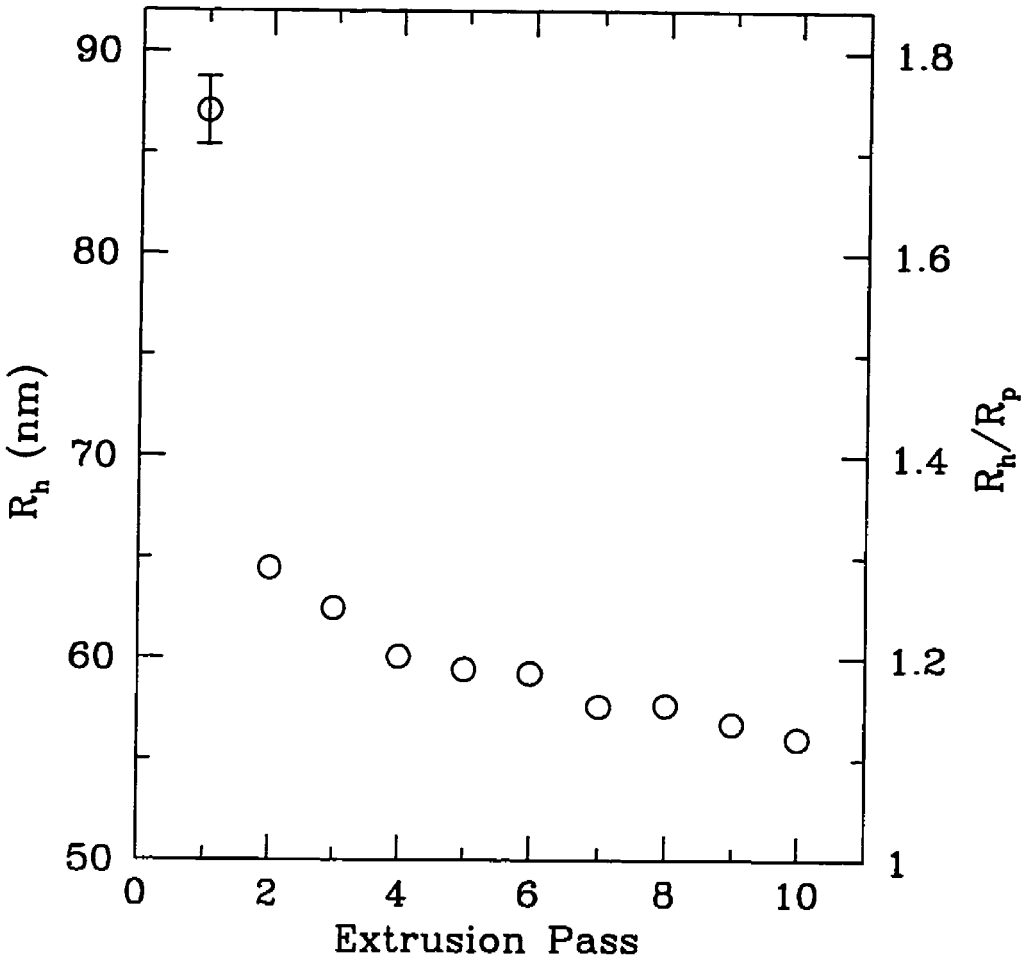

Figure 4.4: The mean hydrodynamic radius $\overline{R}_h$ as a function of the number of extrusions for a typical sample of DMPC vesicles, extruded at 200 psi and 30°C. For comparison, the right-hand axis plots the data as the ratio of $\overline{R}_h$ to the pore radius R_p=50 nm.

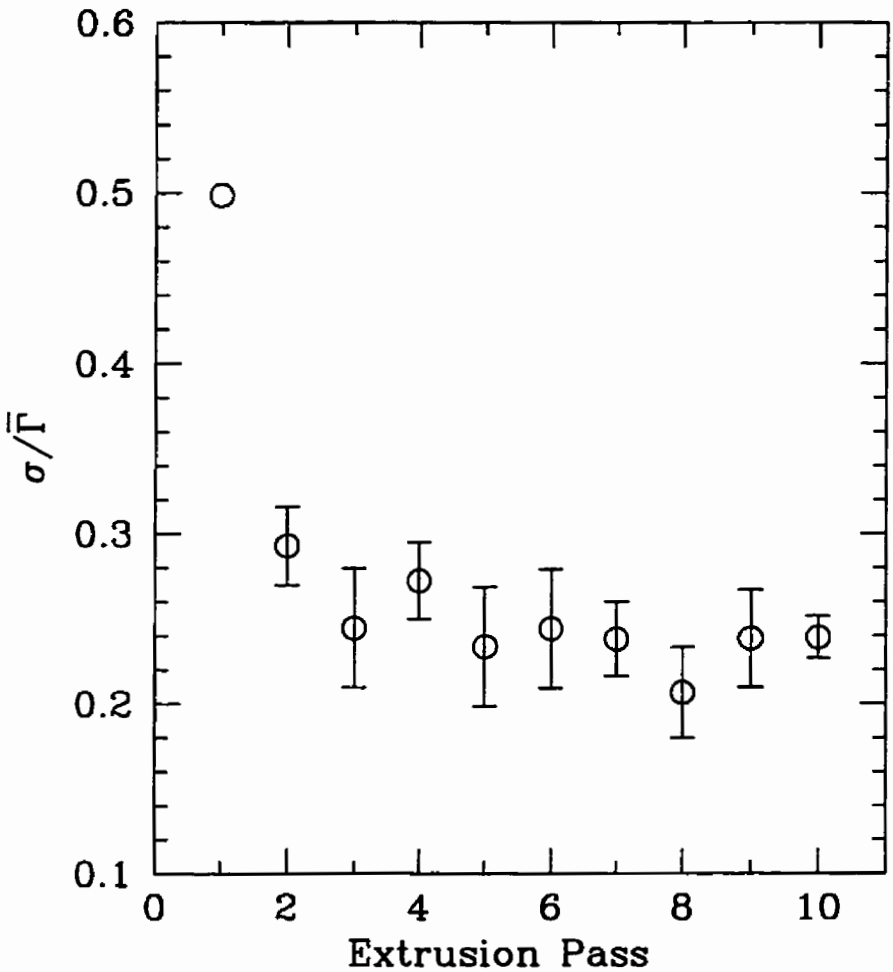

Figure 4.5: The relative standard deviation $\sigma/\overline{\Gamma}$ of the vesicle radius distribution as a function of the number of extrusions for a typical sample of DMPC vesicles, extruded at 200 psi and 30°C.

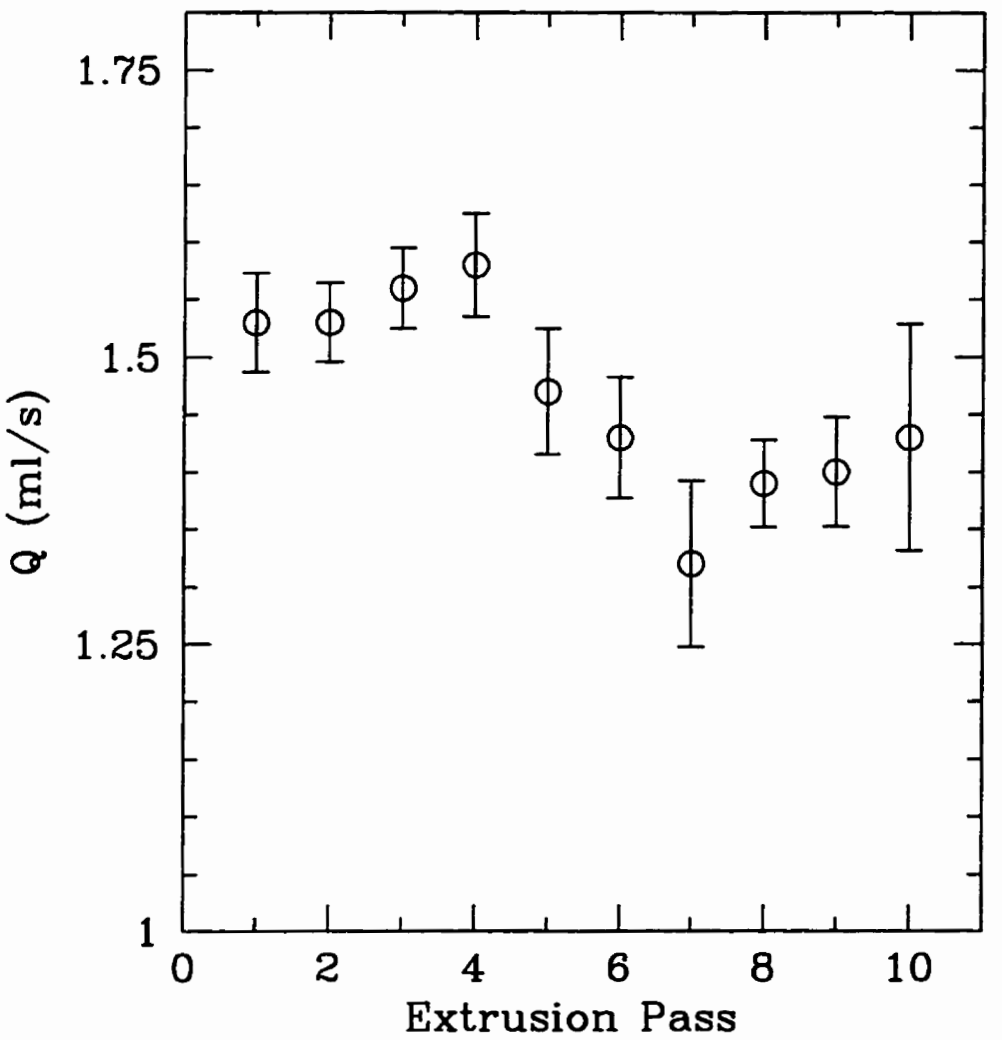

Figure 4.6: The volume flowrate Q as a function of the number of extrusions for a typical DMPC vesicle suspension, extruded at 200 psi and 30°C.

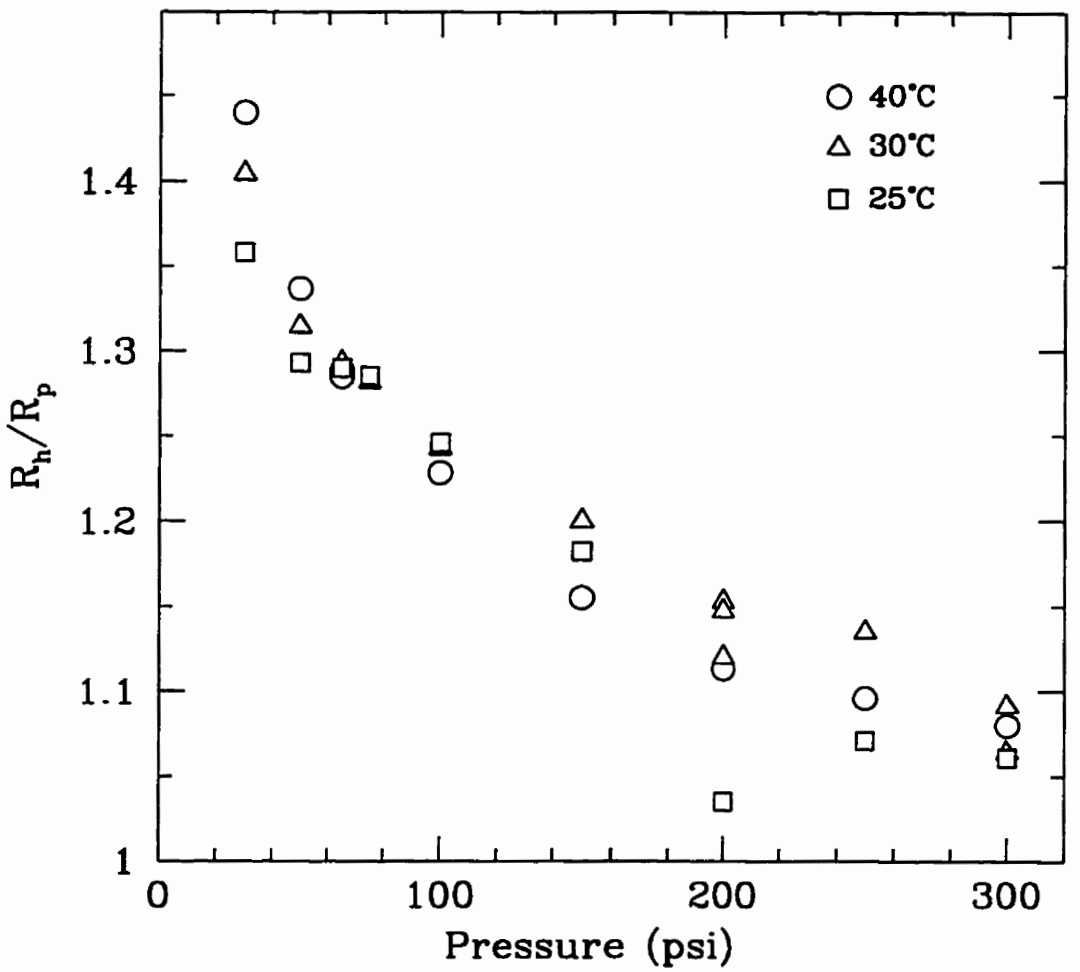

Figure 4.7: Ratio of the mean hydrodynamic radius $\overline{R}_h$ of vesicles to the pore radius R_p=50 nm as a function of extrusion pressure for DMPC vesicles extruded at 25°C, 30°C and 40°C.

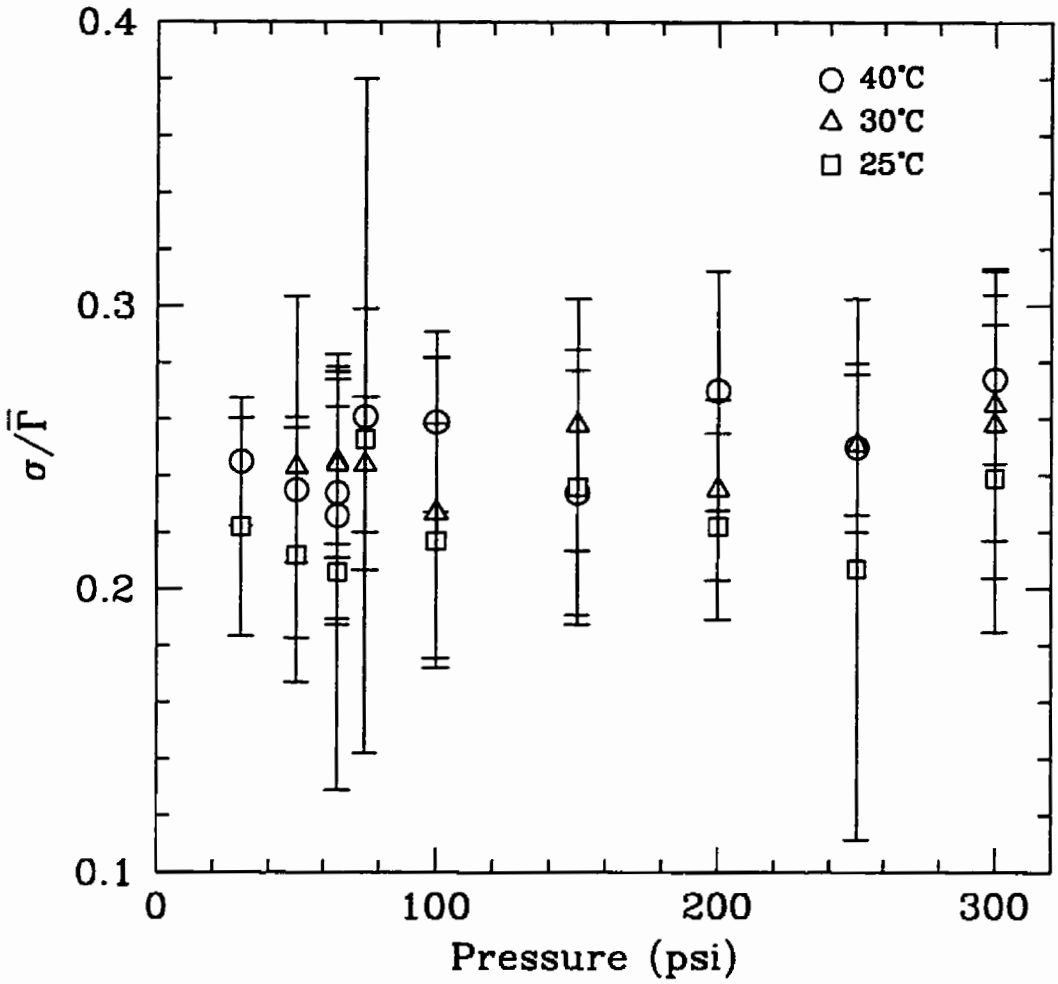

Figure 4.8: The relative standard deviation $\sigma/\bar{\Gamma}$ of the vesicle radius distribution as a function of extrusion pressure for DMPC vesicles extruded at 25°C, 30°C and 40°C.

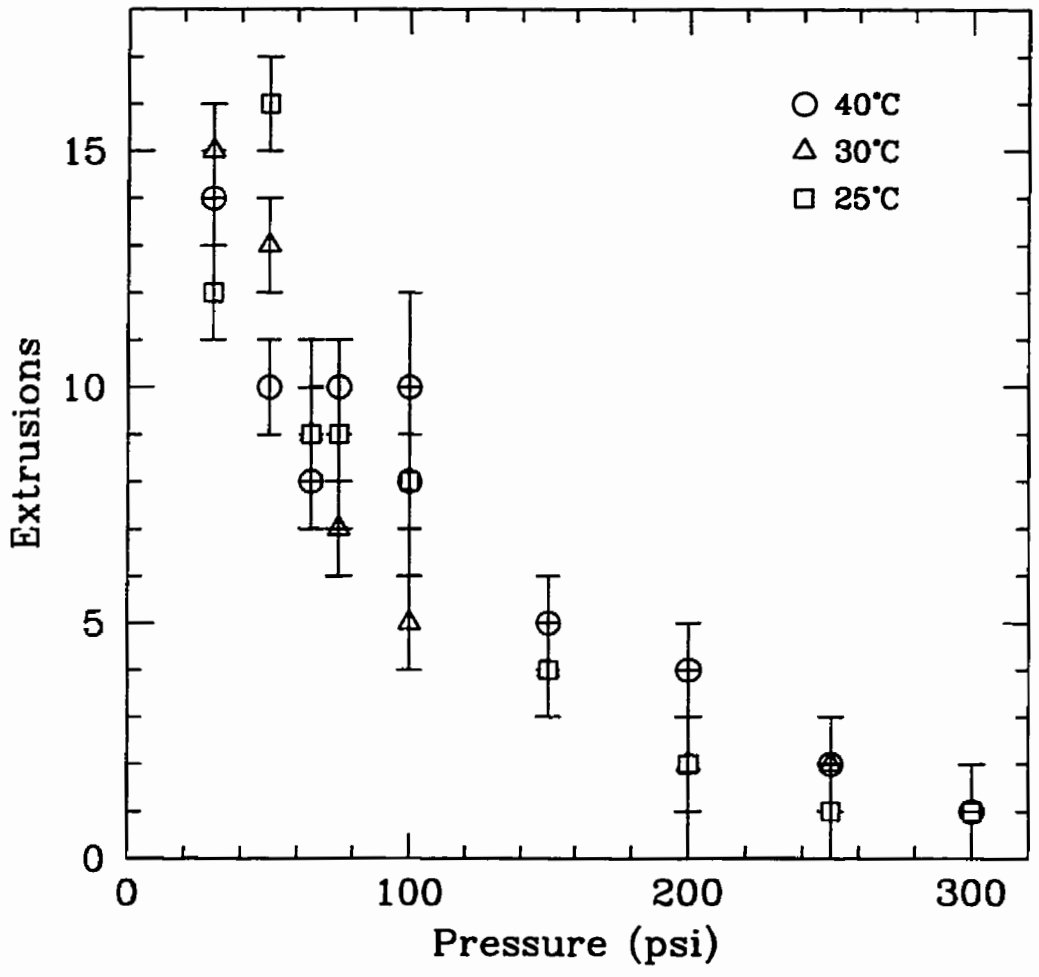

Figure 4.9: The number of extrusions required to reach a steady flowrate as a function of extrusion pressure for DMPC vesicles extruded at 25°C, 30°C and 40°C.

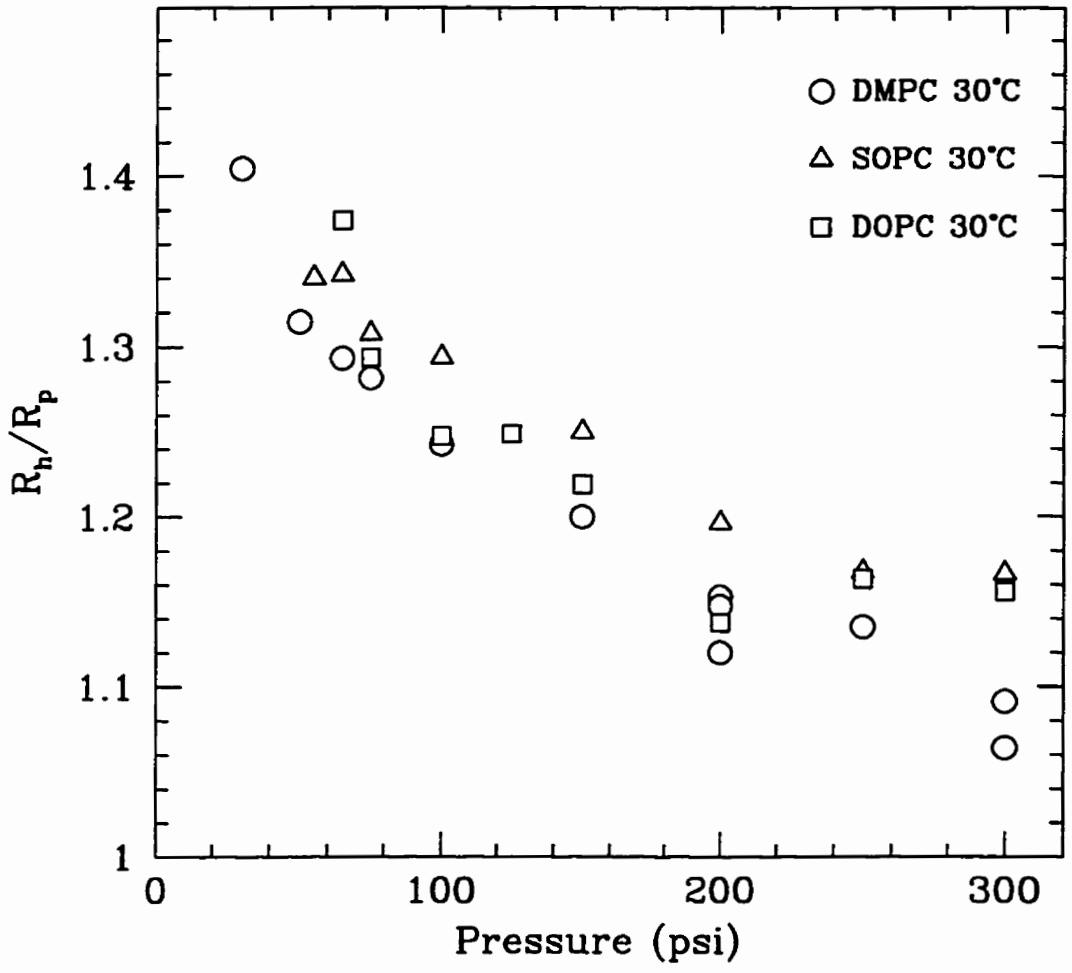

Figure 4.10: Mean hydrodynamic radius of vesicles as a function of extrusion pressure for vesicles composed of either DMPC, SOPC or DOPC. All data shown was taken at a temperature of 30°C.

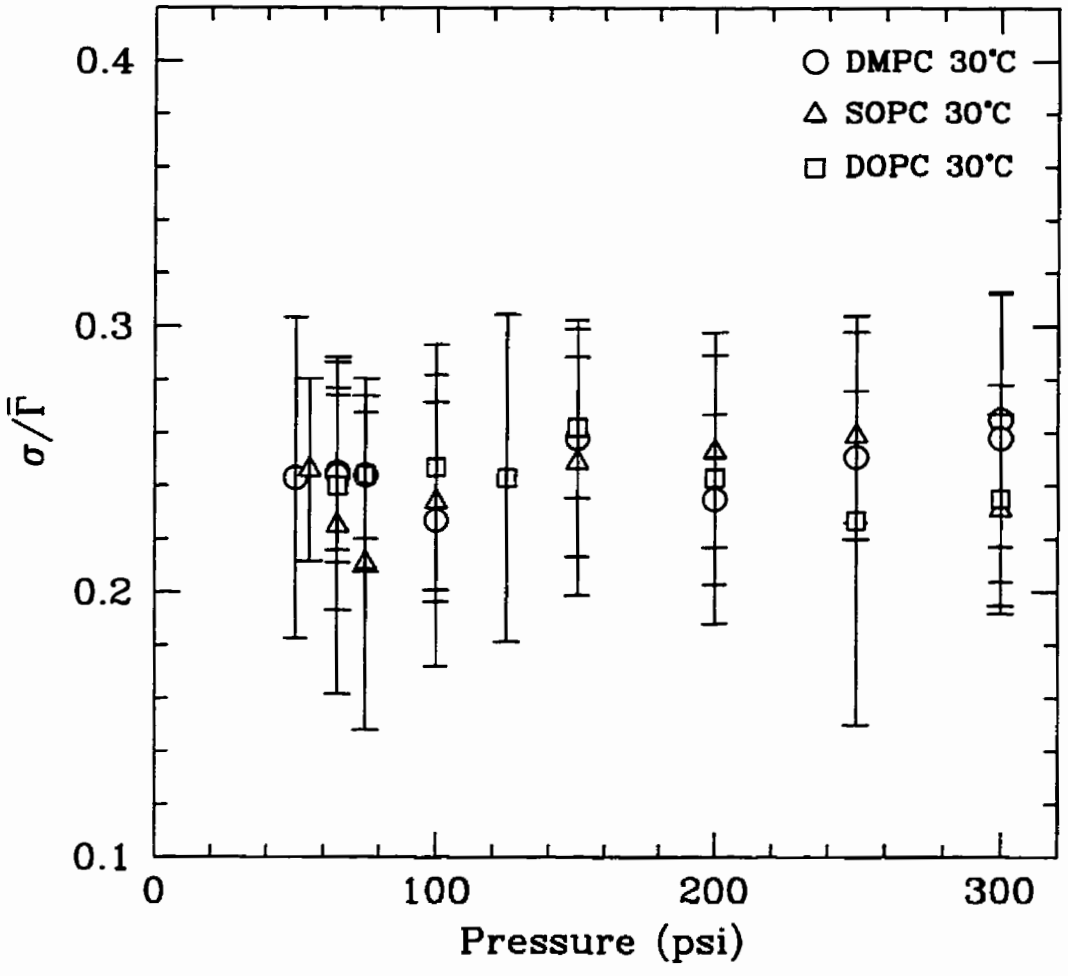

Figure 4.11: Polydispersity of vesicles $\sigma/\overline{\Gamma}$ as a function of extrusion pressure for vesicles composed of either DMPC, SOPC or DOPC. All data shown was taken at a temperature of 30°C.

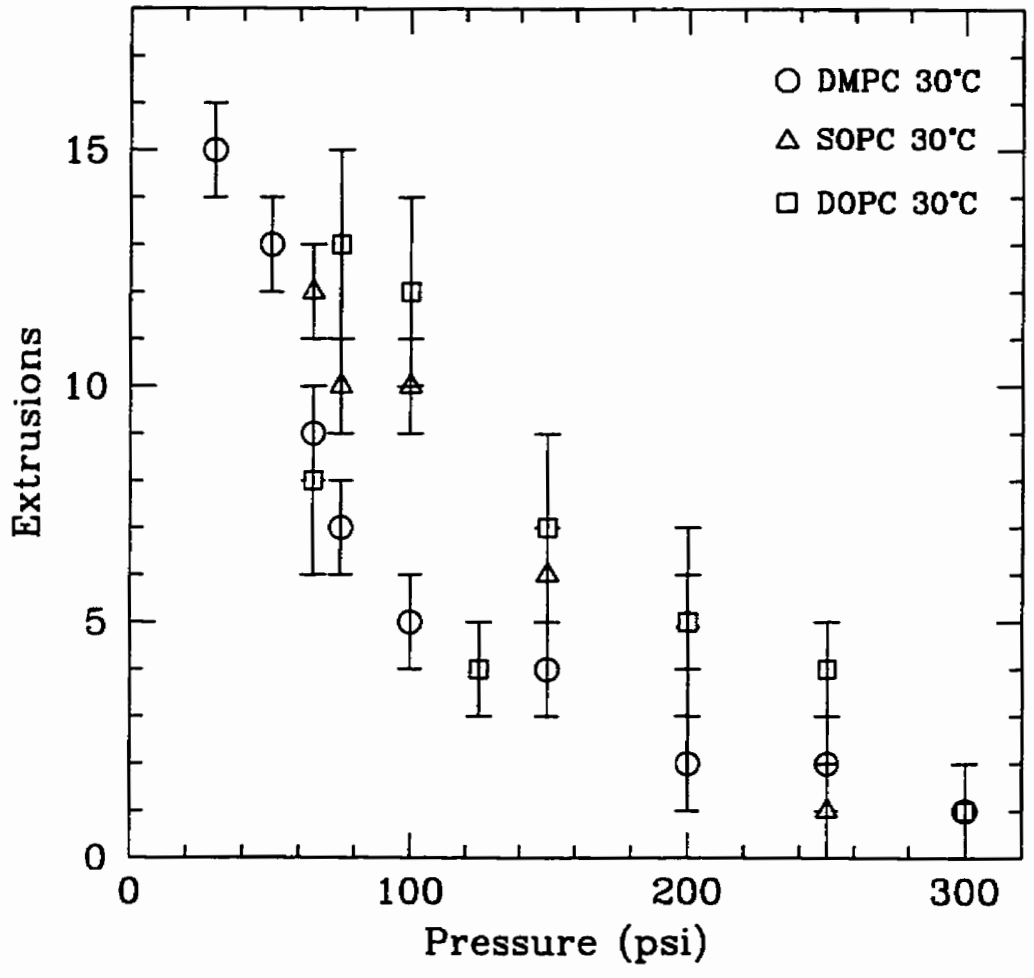

Figure 4.12: The number of extrusions required to reach a steady flowrate as a function of extrusion pressure for vesicles composed of either DMPC, SOPC or DOPC. All data shown was taken at a temperature of 30°C.

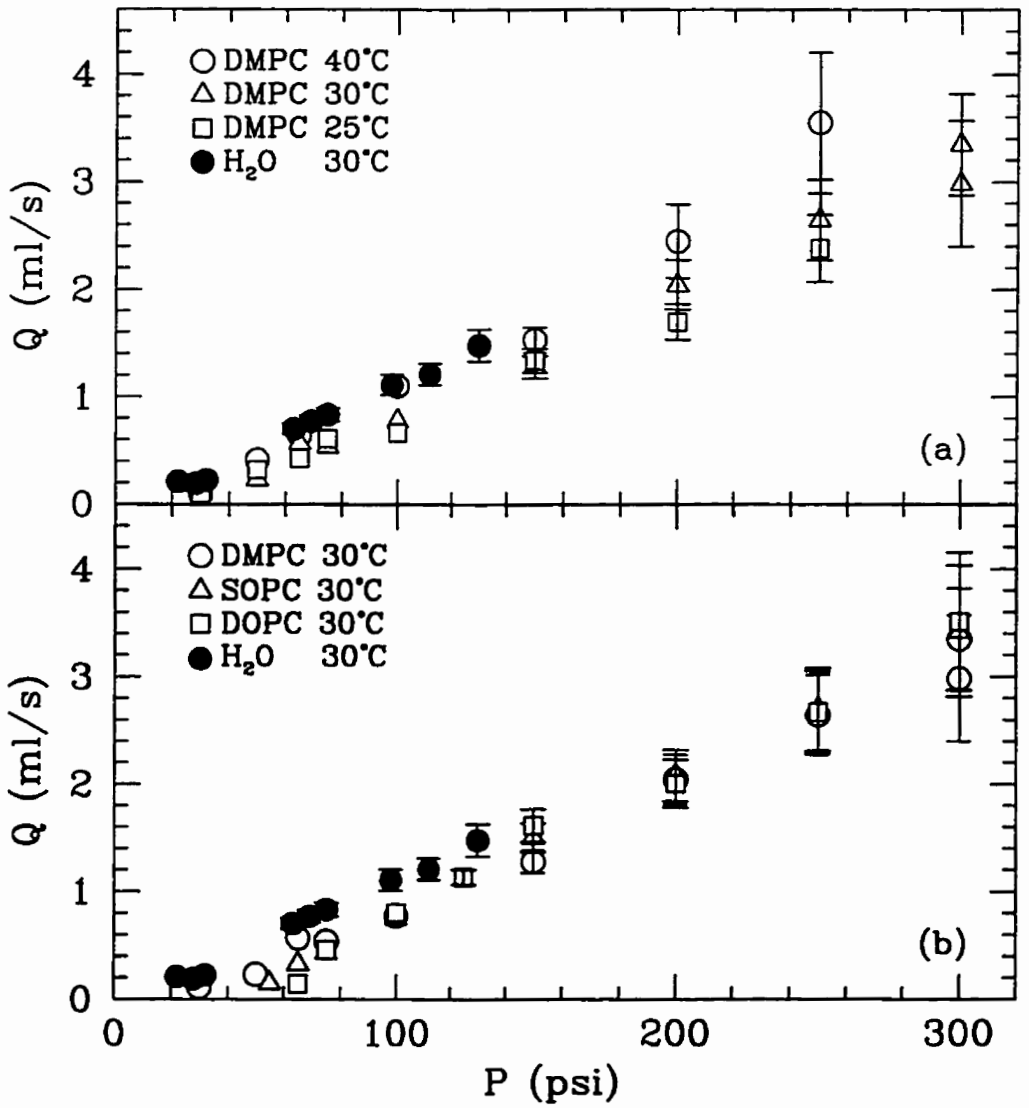

Figure 4.13: The flowrates of vesicle suspensions as a function of extrusion pressure. In both plots the flowrate of pure water has been shown for comparison. (a) The final flowrates of DMPC vesicle suspensions for samples extruded at 25°C, 30°C and 40°C. (b) The final flowrates of DMPC, SOPC and DOPC vesicle suspensions. These samples were all extruded at 30°C.

Chapter 5

Discussion

5.1 Flowrate

As seen in Fig. 4.13, the flowrate of water is proportional to the applied pressure over the entire range of applied pressures as predicted by Darcy's law. The measured flowrate for water is less than that predicted by Eq. 3.4, most likely due to an unknown density of pores. Interestingly, the flowrate of water decreased with increasing number of extrusions at constant pressure, reaching the point of zero flowrate after 4-6 passes. No corresponding decrease of flowrate with number of extrusion passes occurred for vesicle suspensions. On the contrary, the flowrate of the vesicle suspensions increased as the vesicles were cycled through the extruder a number of times eventually equilibrating at a constant flowrate. The vesicles in suspension appear to be facilitating the flow of water through the pores. The reasons for this behaviour are unclear at this time.

At high pressures, the measured flowrates for the different vesicle suspensions are also proportional to the applied pressure. From the slopes of the flowrate at high pressures (> 100 psi), the effective permeability for each vesicle suspension was calculated. The permeability of water was calculated using data over the entire range of pressures. The results are shown in Table 5.1. Within experimental uncertainties, the measured permeabilities of the vesicle suspensions are consistent with that measured for water. This is not very surprising, considering the fact that all of the vesicle

suspensions were made at a very small concentrations of lipid ($\sim$ 1 mg/mℓ). If the boundary layer thickness is known, it is possible to estimate the expected permeability decrease. These calculations are made in section 5.3, where it is found that the permeability decrease is on the order of 0.5%.

Table 5.1: Effective permeability of polycarbonate membranes to vesicle solutions

Sample	Temperature (°C)	Permeability K_{eff} (10^{-15}m^4)
Water (Observed)	25	1.53 $\pm$ 0.08
DMPC	40	1.11 $\pm$ 0.51
DMPC	30	1.37 $\pm$ 0.15
DMPC	25	1.47 $\pm$ 0.25
SOPC	30	1.57 $\pm$ 0.11
DOPC	30	1.52 $\pm$ 0.20

The temperature dependence of the flowrates measured for different vesicle solutions appears to be due solely to differences in the viscosity of water at different temperatures. This is can be seen in Fig. 5.1 which shows the viscosity-corrected flowrate (the product of the flowrate of the suspension with the viscosity of water at the temperature of extrusion) as a function of extrusion pressure for all vesicle suspensions and temperatures studied. The vesicle suspension data are indistinguishable at high extrusion pressures where the viscosity-corrected flowrates of constant lipid concentration vesicle suspensions are independent of temperature or lipid properties. This is consistent with Bruinsma's picture, but not with Gompper and Kroll's.

5.2 Minimum Pressure

The graph inset to Fig. 5.1 shows that variations in the flowrate occur between samples of different lipids at low pressures. There does not seem to be any significant difference in low pressure data for DMPC samples extruded at different temperatures. The pressure at which a suspension's flowrate reaches zero is defined as its minimum extrusion pressure P_{min}.

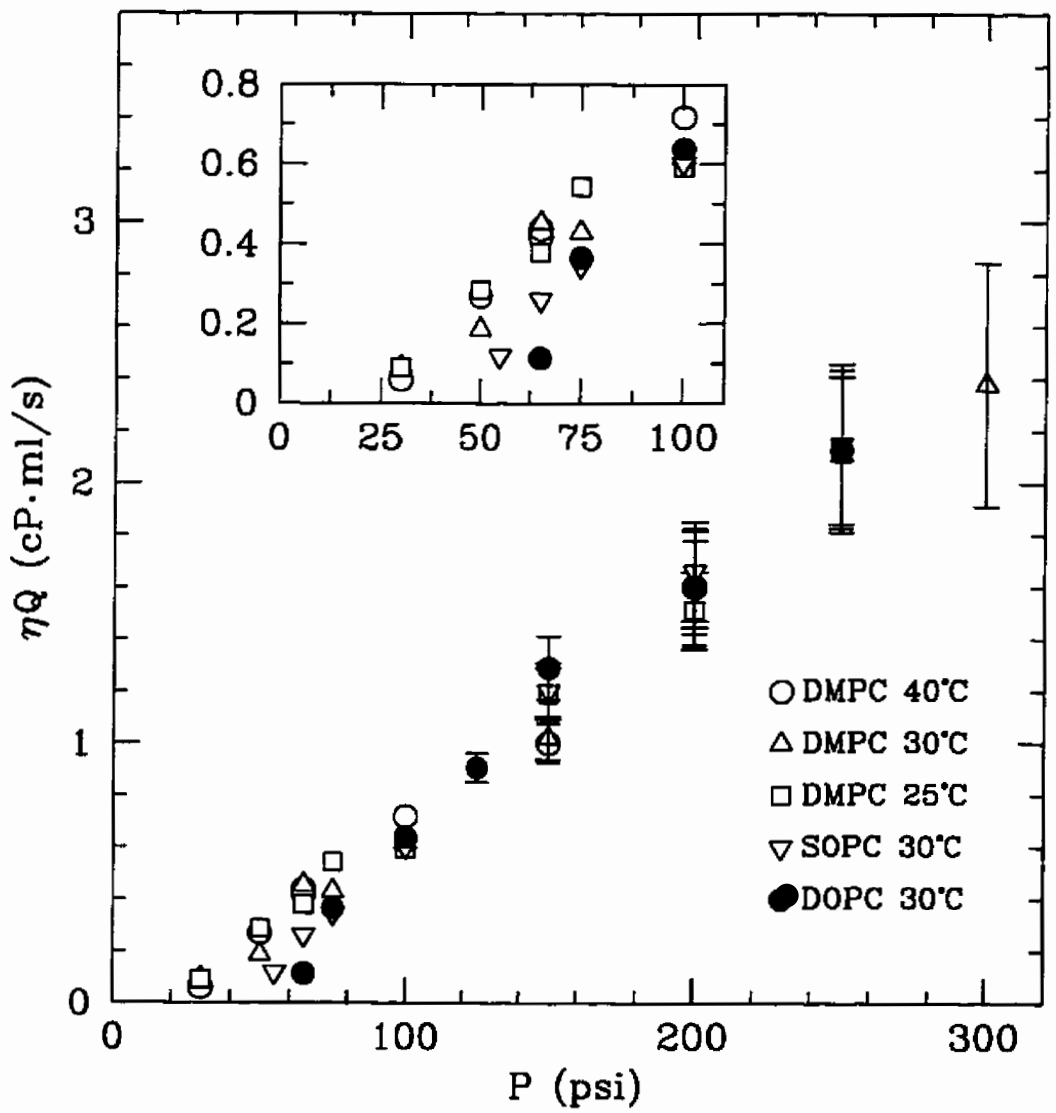

Figure 5.1: The viscosity-corrected final flowrate ηQ as a function of extrusion pressure for all samples studied. The concentration of lipid in solution was 1 mg/mℓ. The inset is a magnified view of the low pressure region which shows the different minimum pressures observed in different lipid solutions.

The minimum extrusion pressures P_{min} for the various samples are determined by fitting the viscosity-corrected flowrate ηQ at low pressures ($\leq$ 100 psi) with an empirical function of the form

$$\eta Q = C(P - P_{min})^{\alpha} , \tag{5.1}$$

where C and α are constants determined by the fitting algorithm. Only points corresponding to pressures at or below 100 psi were used in the fits. Results for P_{min}, C and α are shown in Table 5.2. The exponent α is different for each data set and the data cannot be fit to a single value for α. The results for the minimum pressure for DMPC data sets were obtained by combining the viscosity-corrected flowrate data sets for each temperature and fitting this combined data set.

Table 5.2: Values of fit parameters C, α, and P_{min} resulting from fit of Eq. 5.1 to flowrate as a function of extrusion pressure.

Lipid	C ($\times 10^1$)	α	P_{min} (psi)
DMPC	0.12	0.92	23.1 $\pm$ 7.5
SOPC	1.02	0.52	49.7 $\pm$ 8.6
DOPC	0.36	0.71	63.9 $\pm$ 1.4

Intuitively, it is easy to understand why there should be a minimum pressure to extrude vesicles; however, this observation is addressed only by Gompper and Kroll [4]. The multilamellar vesicle which is being extruded is initially two orders of magnitude larger than the size of the pore, as shown schematically in Fig. 5.2. This vesicle must be deformed at some energy cost to fit into the smaller pore and it must suffer a decrease in volume either by diffusion of water through the membrane or through rupture in order to enter the pore.

The minimum pressure was extrapolated from the final flowrate data instead of the initial flowrate. It might be thought that this would cause some problems for the surface tension calculations which used the initial vesicle size instead of the final size. There are two other considerations which support the validity of the usage of the final flowrate. The first of these is the experimental confirmation of the minimum

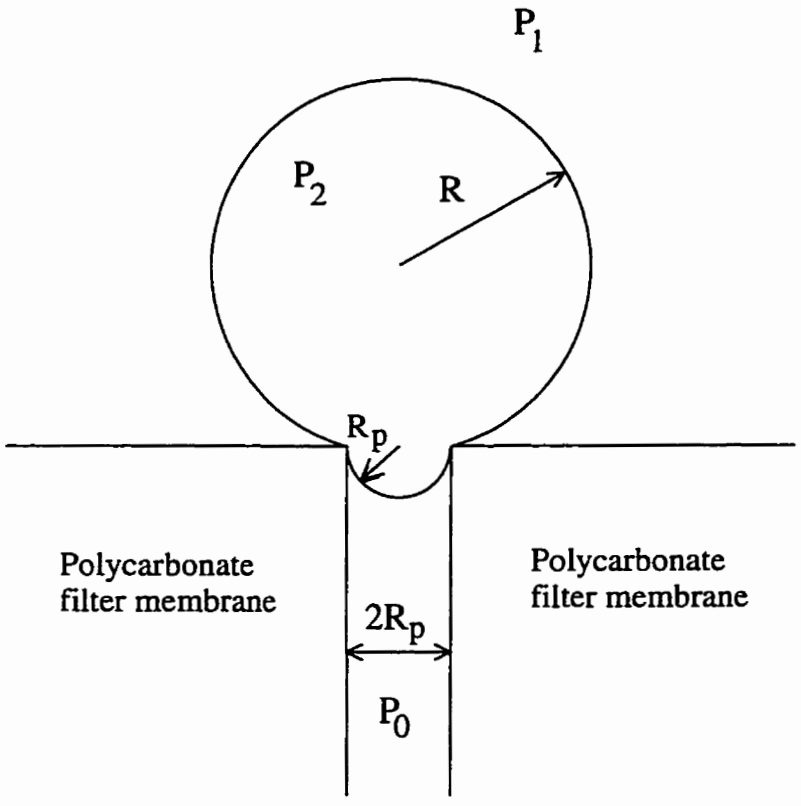

Figure 5.2: A vesicle at the entrance to a pore of radius R_p. The pressure below the vesicle inside the pore is P_0, the pressure above the vesicle is P_1 and the pressure inside the vesicle is P_2. By definition, P_2 is greater than either P_0 and P_1. The diagram is not to scale.

pressures. For each sample, attempts were made to extrude the vesicles at a pressure 10 psi below the lowest reported pressure on the graphs. In each case, the resulting fluid was effectively free of vesicles, thus experimentally confirming the existence of a minimum pressure. The fitted minimum pressures all fall within this observed 10 psi range. The second consideration is that as the pressure of extrusion decreases the size of the final vesicle increases. Hence, as P_{min} is approached, the size of the final vesicles gets larger and larger, decreasing the effect of the vesicle radius R on the surface tension calculations.

The pressure P_b required to bend a vesicle to a given mean radius of curvature R is approximately $P_b \sim 4\pi k_c/R^3$ where k_c is the elastic bending modulus. The pressure required to deform a large DMPC vesicle with a bending modulus of 1.1×10^{-19} J [30]

to fit a pore of radius 50 nm (cf. Fig. 5.2) is roughly 0.13 psi. This is much smaller than any pressure used in the extrusion process so that it appears that energies associated with bending do not limit the extrusion of vesicles.

After it is deformed, the vesicle can decrease in volume by flow of water through the vesicle wall. However, this is a slow process as most, if not all, of the outward water flow occurs across the smaller area inside the pore $2\pi {R_p}^2$. As shown in Appendix C, the time required to decrease the volume of the vesicle sufficiently to fit it into the pore is on the order of 42 minutes, with a resulting required time of 37 hours to extrude a typical 5 mℓ sample. This is much longer than any observed time scale in the extrusion process. On the other hand, the pressure differences across both the large area outside the pore and the small area inside the pore will increase, resulting in the buildup of an effective surface tension in the lipid bilayer as given by the Laplace relation between the pressure difference across a curved interface and the surface tension [45]

$$\Delta P = 2\gamma H + \frac{k_c}{R_p}\left(C_0 - \frac{2}{R_p}\right) , \tag{5.2}$$

where H is the mean curvature of the interface, γ is the surface tension and C_0 is the intrinsic surface curvature. Bilayers which have an identical chemical composition for both monolayers have an intrinsic curvature of zero. It will also turn out that the third term is about 10^8 orders of magnitude smaller than the first, so that it can safely be neglected, leaving only the first term. The pressure is greater on the side of interface where the curvature is positive. For example, a spherical interface will have a greater pressure inside the sphere than outside, as the curvature, in this case the inverse of the radius, is positive inside the sphere.

Now consider again the vesicle shown in Fig. 5.2. Let us assume that the surface tension is constant throughout the bilayer. The pressure "above" the vesicle is given by P_1, the pressure "below" the vesicle, on the exit side of the pore, is P_0 and the pressure inside the vesicle is P_2. In this case, the exit side of the pore is open to the air, so P_0 is equal to the atmospheric pressure. The difference $P_1 - P_0$ is then simply the applied pressure, which is one of our measureable experimental parameters. In the described situation, there is no flow through the pore, as the vesicle is completely

blocking it. All of the pressure drop $P_1 - P_0$ therefore occurs over the vesicle. Now, for the portion of the vesicle exterior to ("above") the pore, the Laplace pressure is given by

$$P_2 - P_1 = \frac{2\gamma}{R} . \tag{5.3}$$

Similarly, the Laplace pressure across the membrane inside the pore is

$$P_2 - P_0 = \frac{2\gamma}{R_p} . \tag{5.4}$$

Subtracting Eq. 5.3 from Eq. 5.4 yields an expression for the pressure difference $P_1 - P_0$ in terms of the pore radius R_p and the radius of the outer portion of the vesicle R

$$P_1 - P_0 = 2\gamma \left[\frac{1}{R_p} - \frac{1}{R} \right] \sim 2\gamma \frac{1}{R_p} . \tag{5.5}$$

If the tension grows larger than the lysis tension of the bilayer, the bilayer will rupture, the contents can escape, and the vesicle will be able to proceed through the pore. Lysis tensions calculated from Eq. 5.5 using values of P_{min} from the fitting of Eq. 5.1 to the viscosity-corrected flowrate data are also shown in Table 5.3. Comparison with values for lysis tensions obtained from pipette aspiration experiments [21] show that the results agree within experimental uncertainties. It appears that the observed minimum pressure required to extrude vesicles is due to the surface tension necessary to cause the vesicles to rupture.

Table 5.3: Rupture tension γ_c of lipid membranes determined by pipette aspiration [32] and minimum extrusion pressure.

Lipid	$P_{min}(psi)$	γ_c by pipette asp. (mN/m) [32]	γ_c by extrusion (mN/m)
DMPC	23.1 $\pm$ 7.5	2.7 $\pm$ 0.8	4.2 $\pm$ 1.4
SOPC	49.7 $\pm$ 8.6	9.0 $\pm$ 1.7	9.0 $\pm$ 1.6
DOPC	63.9 $\pm$ 1.4	10.2 $\pm$ 2.5	11.6 $\pm$ 0.25

5.3 Vesicle Size

Figure 4.4 shows that the size of the extruded vesicles changed rapidly at first, reaching a radius 20% larger than the nominal pore radius in just four extrusions, after which

the rate of size change dropped off. It can be seen from Figs. 4.7 and 4.10 that the size of extruded vesicles decreases with increasing extrusion pressure. This is not very surprising, as one would intuitively expect the vesicles to get smaller as the force applied is increased. (Try varying how hard you blow with a child's soap bubble toy!) There does not seem to be any dependence on the lipid composition of the vesicles or on temperature. The smallest observed vesicle sizes, which occurred at a pressure of 300 psi, is slightly larger than the nominal pore size.

The observation that vesicle size decreases with flowrate is consistent with other studies of complex fluids under shear [57, 58]. These studies show that the size of structures produced decrease with increasing shear rate, which is most directly related to our flowrate instead of pressure. Certainly, as the flow rate increases, Eq. 3.8 predicts that the lubrication layer should increase in thickness so that the vesicle tube decreases in radius. The boundary layer thickness can be estimated using the result of Clerc and Thompson which predicts that the radius of the final vesicle should be 1.77 times that of the cylindrical lamella from which it formed.[1] Assuming that this is correct and looking at the sizes of the extruded vesicles, it can be seen that the cylinders which would have been inside the pores must have been much smaller than the size of the pores. Neglecting the thickness of the bilayer, the radius of a cylindrical lamella in a pore is equal to the radius of the pore R_p minus the boundary layer thickness h^*. The radius of the lamella is also equal to the radius of the final vesicle R_v (taken here as equal to the mean hydrodynamic radius $\overline{R}_h$) divided by 1.77. Therefore, the boundary layer thickness is given by

$$h^* = R_p - \frac{R_v}{1.77} \equiv R_p - \frac{\overline{R}_h}{1.77} \,. \tag{5.6}$$

Using the observed hydrodynamic radii $\overline{R}_h$ of extruded vesicles for R_v and a pore radius R_p of 50 nm, the boundary layer thickness can be calculated. This estimate of h^* may then be used to calculate the expected permeability reduction using Eq. 3.7. The number of vesicles per unit length in a pore n at any given time is also needed for this computation. At the concentrations used in these experiments (1 mg/mℓ),

[1] It would be better to use Bruinsma's formula, but our data leaves too many parameters unknown to do this.

we estimate that there are approximately 0.7 vesicles per pore during the extrusion process, which translates to 0.061 vesicles per micron. This number was arrived at by calculating the number of vesicles per unit volume using the initial phospholipid concentration and an estimated final vesicle radius of 50 nm, and multiplying by the volume of a pore. The results of the calculations of h^*, L^* and K_{eff}/K are shown in Table 5.4. The spherocylinder length is determined by area conservation from the final vesicle size R_v, the pore size R_p and the boundary layer thickness h^*. The resulting equation for L^* is

$$L^* = \frac{2}{r}\left(R_v^2 - r^2\right) , \tag{5.7}$$

where $r = R_p - h^*$. The smallest boundary layer thickness is 9.4 nm, ranging up to a maximum of 20.8 nm. It is apparent from these figures that Bruinsma's assumption that the boundary layer is small compared to the pore radius is not valid. On the other hand, the calculated decrease in the filters' permeability is very small, being on the order of 0.5%. This is in agreement with the observed permeabilities of Table 5.1. The smallness of the decrease is due to the low vesicle density (in turn due to the low lipid concentration), which leads to the number of vesicles per pore n being small. For higher concentrations, a larger decrease in permeability might be expected.

Another interesting computation is that of the surface tension of the front of a vesicle inside a pore. Using the boundary layer just calculated in conjunction with Eq. 3.8 and the volume flowrate Q, the surface tension γ can be calculated. The results of these calculations are shown in Table 5.5. Since the vesicles are rupturing at some point, it is reasonable to assume that the surface tension of the vesicles should be at least the same order of magnitude as the rupture tension for the given type of lipid membrane. The surface tensions calculated are smaller than expected, but are approaching the correct order of magnitude. It must not be forgotten that these numbers were derived from Bruinsma's equations for steady-state flow, with no allowances for rupture and ignoring the fact that the assumption that the lubrication layer thickness is negligible compared with the veiscle radius is not valid. Given this, it is not unexpected that there will be some deviation from experiment. Indeed, it is surprising that the results agree as well as they do.

5.4 Polydispersity

Of considerable interest is the observation that there is no improvement in the relative polydispersity as the extrusion pressure is increased. This is somewhat counter-intuitive, as one might expect to achieve more uniformity of the vesicle population as the applied force is increased. Such an improvement with increasing shear force has been observed in oil-water-surfactant systems by Mason and Bibette [57]. A clue to the reasons for this may be found in the elctron microscope photographs of the surface of the polycarbonate filters (cf. Fig. 4.1) used to extrude the vesicles. As discussed in Chapter 4, the pores vary widely in size, with some pores apparently being twice the manufacturer's stated maximum size. Since the size of a vesicle is dependent on the size of the pore through which it is extruded, it is reasonable to expect varying pore sizes to limit the degree to which the polydispersity can be reduced.

Table 5.4: Calculated ratios of effective permeability to geometrical permeability K_{eff}/K for polycarbonate filters from observed DMPC vesicle sizes, along with final vesicle sizes R_v, boundary layer thicknesses h^* and the spherocylinder length L^*. The boundary layer thickness and spherocylinder length were calculated using Eqs. 5.6 and 5.7, respectively.

P (psi)	R_v (nm)	h^* (nm)	L^* (nm)	K_{eff}/K
DMPC vesicles extruded at 40°C				
30.0	72.01	9.37	174	0.994
50.0	66.85	12.3	162	0.995
65.0	64.41	13.7	156	0.995
65.0	64.24	13.8	155	0.995
100.0	61.42	15.6	148	0.995
150.0	57.76	17.4	140	0.996
200.0	55.67	18.6	135	0.996
250.0	54.80	19.1	132	0.996
300.0	54.00	19.5	131	0.996
DMPC vesicles extruded at 30°C				
30.0	70.22	10.4	170	0.995
50.0	65.73	12.9	159	0.995
65.0	64.67	13.5	156	0.995
75.0	64.09	13.8	155	0.995
100.0	62.14	14.9	150	0.995
150.0	60.00	16.2	145	0.995
200.0	57.65	17.5	139	0.996
200.0	57.38	17.6	139	0.996
200.0	56.01	18.4	135	0.996
250.0	56.76	18.0	137	0.996
300.0	54.57	19.2	132	0.996
300.0	53.21	20.0	129	0.996
DMPC vesicles extruded at 25°C				
30.0	67.92	11.7	164	0.995
50.0	64.65	13.5	156	0.995
65.0	64.50	13.6	156	0.995
75.0	64.27	13.7	155	0.995
100.0	62.29	14.9	151	0.995
150.0	59.12	16.7	143	0.995
200.0	51.75	20.8	125	0.996
250.0	53.55	19.7	129	0.996
300.0	53.05	20.1	128	0.996

Table 5.4 (Continued).

P (psi)	R_v (nm)	h^* (nm)	L^* (nm)	K_{eff}/K
SOPC vesicles extruded at 30°C				
55.0	67.02	12.2	162	0.995
65.0	67.12	12.1	162	0.995
75.0	65.39	13.1	158	0.995
100.0	64.70	13.5	156	0.995
150.0	62.51	14.7	151	0.995
200.0	59.83	16.2	145	0.995
250.0	58.38	17.1	141	0.996
300.0	58.32	17.1	141	0.996
DOPC vesicles extruded at 30°C				
65.0	68.70	11.2	166	0.995
75.0	64.68	13.5	156	0.995
100.0	62.39	14.8	151	0.995
125.0	62.45	14.8	151	0.995
150.0	60.96	15.6	147	0.995
200.0	56.89	17.9	138	0.996
250.0	58.17	17.2	141	0.996
300.0	57.80	17.4	140	0.996

Table 5.5 (Continued).

Table 5.5: Calculated tensions γ of vesicle frontcaps, with corresponding final vesicle size R_v, boundary layer thickness h^* (from Eq. 5.6 and viscosity-corrected flowrate ηQ. The vesicle size and viscosity-corrected flowrate were determined experimentally. The endcap surface tension γ was calculated from these data using Eq. 3.8.

P (psi)	R_v (nm)	h^* (nm)	ηQ (cP·mℓ/s)	γ (mN/m)
DMPC vesicles extruded at 40°C				
30.0	72.01	9.37	0.0591	0.173
50.0	66.85	12.3	0.269	0.523
65.0	64.41	13.7	0.437	0.725
65.0	64.24	13.8	0.418	0.686
100.0	61.42	15.4	0.718	1.00
150.0	57.76	17.4	1.00	1.15
200.0	55.67	18.6	1.60	1.67
250.0	54.80	19.1	2.32	2.33
DMPC vesicles extruded at 30°C				
30.00	70.22	10.4	0.0904	0.226
50.00	65.73	12.9	0.186	0.336
65.00	64.67	13.5	0.453	0.764
75.00	64.09	13.8	0.430	0.700
100.0	62.14	14.9	0.618	8.97
150.0	60.00	16.2	1.02	1.32
200.0	57.65	17.5	1.63	1.87
200.0	57.38	17.6	2.11	2.39
200.0	56.01	18.4	2.38	2.53
250.0	56.76	18.0	2.67	2.94
DMPC vesicles extruded at 25°C				
30.00	67.92	11.7	0.0891	0.187
50.00	64.65	13.5	0.285	0.480
65.00	64.50	13.6	0.379	0.6.32
75.00	64.27	13.7	0.543	0.893
100.0	62.29	14.9	0.592	0.866
150.0	59.12	16.7	1.19	1.47
200.0	51.75	20.8	1.51	1.33
250.0	53.55	19.8	2.12	2.02

P (psi)	R_v (nm)	h^* (nm)	ηQ (cP·mℓ/s)	γ (mN/m)
SOPC vesicles extruded at 30°C				
55.00	67.02	12.2	0.118	0.232
65.00	67.12	12.1	0.260	0.516
75.00	65.39	13.1	0.345	0.609
100.0	64.70	13.5	0.602	1.02
150.0	62.51	14.7	1.20	1.78
200.0	59.83	16.2	1.66	2.12
250.0	58.38	17.1	2.15	2.56
300.0	58.32	17.1	2.73	3.24
DOPC vesicles extruded at 30°C				
65.00	68.70	11.2	0.113	0.251
75.00	64.68	13.5	0.365	0.616
100.0	62.39	14.8	0.638	0.939
125.0	62.45	14.8	0.906	1.34
150.0	60.96	15.6	1.29	1.75
200.0	56.89	17.9	1.60	1.77
250.0	58.17	17.2	2.13	2.51
300.0	57.80	17.4	2.80	3.24

Chapter 6

Conclusions

Our objective in this work was to understand better how unilamellar vesicles are formed by extrusion. This would be helpful from the point of view of gaining insight into the properties and behaviour of phospholipid bilayers and vesicles in non-equilibrium and non-steady states. The empirical data gathered also has applications for researchers using vesicles in the lab and for the industrial production of vesicles containing pharmaceuticals. The means of accomplishing this goal that we chose was to characterise the end products of extrusion as a function of the lipid composition, applied pressure and extrusion temperature.

The central observation of this study is that there exists a minimum pressure to extrude a suspension of vesicles in water through the filter membrane. This minimum pressure is dependent on the properties of the lipid composing the vesicles, but not on the bending rigidity, as has been suggested previously [4]. Instead, the minimum pressure seems to be a linear function of the lysis tension of the phospholipid bilayer. Lysis tensions computed from the minimum pressures agree, within experimental error, with other methods [21]. Determination of the minimum pressure is thus a convenient method of measuring the lysis tension of a phospholipid.

It was also observed that the flowrate of the solution increased and the size of the extruded vesicles decreased as the applied pressure was increased. This is consistent with other studies of complex fluids under shear [57, 58]. Above the region of pressure space near the minima (> 100 psi), the pressure dependence of the viscosity-corrected

flowrates of all the samples are linear and equal, with no apparent effects due to the lipid composition. This lack of dependence of flowrate on lipid properties is in agreement with the results of Bruinsma [5]. The dependence of flowrate on concentration remains to be determined. The flowrate and vesicle size data were used to estimate the decrease in filter permeability and the vesicle surface tension while inside the pore. The permeability estimates agreed with the experimental results within uncertainties, but the permeability decreases are small due to the low concentration of vesicles present, making a clear verification of Bruinsma's model difficult. The predicted surface tensions are only within an order of magnitude of the appropriate lysis tensions. Given the approximations of the model, this is quite a reasonable degree of agreement. Any future model needs to consider the necessity of the vesicle rupturing and what might occur after such an event. The primary effect of the temperature was to change the viscosity of the water.

Surprisingly, the polydispersity of the samples did not decrease with increasing numbers of extrusions or with increasing pressure. Our primary hypothesis for this is that decreases in the polydispersity are limited by the wide variation in the sizes of the pores in the polycarbonate filter membranes. The manufacturer's claims and actual sample filter pore measurements conflict with each other. Direct measurements of the pore sizes and size distributions of the polycarbonate filter membranes by electron microscopy are probably the best way to resolve this, but this requires considerable effort and patience to develop the necessary sample preparation skill. A distribution function for the pore sizes would be very helpful in shedding light on the origin of the sample polydispersity. This might be determined by a careful analysis of the electron microscopy photos. It would be even more helpful if more monodisperse filter membranes could be manufactured.

As stated above, the limiting factor to pushing vesicles through pores is the pressure required to cause them to break open. Once they break open, they are able to enter the pore, but how they re-form themselves into smaller vesicles is unclear. From the models of Clerc and Thompson [3] and Bruinsma [5], however, a very basic hypothesis of the mechanism can be pieced together. The vesicles do not move into the pore until they break. When they do break, the opening will form in the part

of the vesicle inside the pore as this is the portion of the membrane surface under the most stress. The vesicle is pushed into the pore, forming cylindrical lamellae, separated from the pore wall by the boundary layer of water required by viscous flow. The thickness of this boundary layer is a function of the pressure indirectly through the flowrate. The boundary layer thickness in turn determines the radius of the cylindrical lamella. The lamella is under stress due to the shear force of the water flowing past the exterior, which causes the cylindrical form to be unstable to a form of the Rayleigh instability. This instability causes the vesicles to break up into the smaller vesicles which are observed.

We operated under the assumption that when the volume flowrate of the extruded suspension stopped changing, the size of the vesicles also stopped changing. While this was consistent with our observations, some work to clarify this matter is necessary. Whether or not the Rayleigh instability is applicable here is questionable, as Rayleigh's instability assumes a small perturbation to a steady state system. Extrusion is not a steady state phenomenon. If the Rayleigh instabilty is applicable to this system, the fastest growing mode of instability for the system should be determined, as the $\lambda = 2\pi R$ criterion is merely the stability limit. The fact that the vesicles do rupture should be taken into account in any future model, as should the fact that the minimum pressure depends on the lysis tension rather than the bending rigidity.

Appendix A

Derivation of the Scattered Electric Field

The equation for the scattered electric field may be derived using Maxwell's equations. This derivation follows that given by Berne and Pecora [9], which in turn follows the treatment of Landau and Lifshitz (1960) [59]. More complete information on Maxwell's equations can be found there. The treatment here places considers that the scattering event occurs in a medium rather than *in vacuo* as is done in Ref. [9].

Maxwell's equations, in their most general forms, are

$$\begin{aligned} \nabla\cdot\mathbf{D} &= \rho \quad \nabla\times\mathbf{H} = \mathbf{J} + \frac{\partial\mathbf{B}}{\partial t} \\ \nabla\cdot\mathbf{B} &= 0 \quad \nabla\times\mathbf{E} = -\frac{\partial\mathbf{B}}{\partial t}\,. \end{aligned} \tag{A.1}$$

Here, $\mathbf{E}$ is the electric field, $\mathbf{B}$ is the magnetic flux density, $\mathbf{D}$ is the dielectric displacement field and $\mathbf{H}$ is the magnetic field. In the problem at hand, the scattering medium is nonconducting and nonmagnetic, with the result that $\rho = 0$, $\mathbf{J} = 0$ (no free charges in the medium), and $\mathbf{H} = \mathbf{B}/\mu_o$ (no magnetisation of the medium).

Consider a medium with a local dielectric constant tensor

$$\underline{\varepsilon} = \varepsilon\underline{\mathbf{I}} + \delta\underline{\varepsilon}\,, \tag{A.2}$$

where ε is the average dielectric constant of the medium and $\delta\underline{\varepsilon}$ gives the tensor form of the fluctuations about the average. It must be noted that the scattered fields are

much lower in amplitude than the incident fields. The magnitude of the dielectric fluctuations is also small compared to the average.

The electric, dielectric displacement, and magnetic fields of the incident plane wave are $\mathbf{E}_i$, $\mathbf{D}_i$, and $\mathbf{H}_i$, respectively. Similarly, the scattered fields are $\mathbf{E}_s$, $\mathbf{D}_s$, and $\mathbf{H}_s$. The totals of the fields at any given point in the medium are then

$$\mathbf{E} = \mathbf{E}_i + \mathbf{E}_s \tag{A.3}$$

$$\mathbf{D} = \mathbf{D}_i + \mathbf{D}_s \tag{A.4}$$

$$\mathbf{H} = \mathbf{H}_i + \mathbf{H}_s \tag{A.5}$$

(A.6)

Since ($\mathbf{E}$, $\mathbf{D}$, $\mathbf{H}$) and ($\mathbf{E}_i$, $\mathbf{D}_i$, $\mathbf{H}_i$) satisfy Maxwell's equations, ($\mathbf{E}_s$, $\mathbf{D}_s$, $\mathbf{H}_s$) must also do so. Therefore, Maxwell's equations for this particular problem are

$$\nabla \times \mathbf{E}_s = -\frac{\partial \mathbf{H}_s}{\partial t} , \tag{A.7}$$

$$\nabla \times \mathbf{H}_s = \frac{\partial \mathbf{D}_s}{\partial t} , \tag{A.8}$$

$$\nabla \cdot \mathbf{D}_s = 0 \text{ , and} \tag{A.9}$$

$$\nabla \cdot \mathbf{H}_s = 0 . \tag{A.10}$$

(A.11)

The scattered magnetic field $\mathbf{H}_s$ can be eliminated by taking the curl of Eq. A.7 and substituting Eq. A.8 into it

$$\nabla \times \nabla \times \mathbf{E}_s = -\frac{\partial^2 \mathbf{D}_s}{\partial t^2} . \tag{A.12}$$

The total displacement vector $\mathbf{D}$ is related to the total electric field vector $\mathbf{E}$ by the relation

$$\begin{aligned} \mathbf{D} &= \underline{\varepsilon} \cdot \mathbf{E} \\ &= (\varepsilon \underline{\mathbf{I}} + \delta \underline{\varepsilon}) \cdot (\mathbf{E}_i + \mathbf{E}_s) \qquad \text{(A.13)} \\ &= \varepsilon \mathbf{E}_i + (\delta \underline{\varepsilon}) \cdot \mathbf{E}_i + \varepsilon \mathbf{E}_s + (\delta \underline{\varepsilon}) \cdot \mathbf{E}_s . \end{aligned}$$

(A.14)

Expanding this using Eq. A.4 and the fact that $\mathbf{D}_i = \varepsilon \mathbf{E}_i$ gives

$$\mathbf{D}_s = \varepsilon \mathbf{E}_s + (\delta \underline{\varepsilon}) \cdot \mathbf{E}_i \ , \tag{A.15}$$

neglecting the second order term $(\delta \underline{\varepsilon}) \cdot \mathbf{E}_s$. The scattered electric field $\mathbf{E}_s$ is then

$$\mathbf{E}_s = \frac{1}{\varepsilon} \mathbf{D}_s - \frac{\delta \underline{\varepsilon}}{\varepsilon} \cdot \mathbf{E}_i \ . \tag{A.16}$$

We are now in a position to substitute Eq. A.16 into Eq. A.12 to get a wave equation

$$\nabla \times \nabla \times (\mathbf{D}_s - (\delta \underline{\varepsilon}) \cdot \mathbf{E}_i) = -\varepsilon \frac{\partial^2 \mathbf{D}_s}{\partial t^2} \ . \tag{A.17}$$

Using the vector identity $\nabla \times \nabla \times \mathbf{A} = \nabla(\nabla \cdot \mathbf{A}) - \nabla^2 \mathbf{A}$, we notice that $\nabla \cdot \mathbf{D_s} = 0$, leaving only the Laplacian of $\mathbf{D}_s$, so that Eq. A.17 becomes

$$\nabla^2 \mathbf{D_s} - \varepsilon \frac{\partial^2 \mathbf{D}_s}{\partial t^2} = -\nabla \times \nabla \times ((\delta \underline{\varepsilon}) \cdot \mathbf{E}_i) \ . \tag{A.18}$$

This wave equation has an inhomogeneous source term, which makes solving the equation difficult. The problem can be simplified by defining a new vector, $\boldsymbol{\pi}$ (the Hertz vector), where

$$\mathbf{D}_s = \nabla \times \nabla \times \boldsymbol{\pi} \ . \tag{A.19}$$

If Eq. A.19 is substituted in Eq. A.18, it is can be shown that the Hertz vector satisfies a wave equation with the simple source term $-(\delta \underline{\varepsilon}) \cdot \mathbf{E}_i$,

$$\nabla^2 \boldsymbol{\pi} - \varepsilon \frac{\partial^2 \boldsymbol{\pi}}{\partial t^2} = -(\delta \underline{\varepsilon}) \cdot \mathbf{E}_i \ , \tag{A.20}$$

the formal solution of which is

$$\boldsymbol{\pi}(R, t) = \frac{1}{4\pi} \int_v d^3 r \frac{\delta \underline{\varepsilon}(\mathbf{r}, t')}{|\mathbf{R} - \mathbf{r}|} \cdot \mathbf{E}_i(\mathbf{r}, t') \ , \tag{A.21}$$

where t' is the retarded time

$$t' = t - \frac{\sqrt{\varepsilon}}{c} |\mathbf{R} - \mathbf{r}| \ . \tag{A.22}$$

The retarded time t' is the time at which the radiation detected at position $\mathbf{R}$ at time t was emitted at position $\mathbf{r}$.

Now, Eq. 2.1 for $\mathbf{E}_i$ is substituted into Eq. A.21

$$\pi(\mathbf{R},t) = \frac{1}{4\pi}\int_V d^3r \frac{\delta\underline{\varepsilon}(\mathbf{r},t')}{|\mathbf{R}-\mathbf{r}|}\cdot\hat{\mathbf{n}}_i E_o \exp i(\mathbf{k}_i\cdot\mathbf{r}-\omega_i t') \ . \tag{A.23}$$

The scattered displacement vector is obtained by using Eq. A.23 in the definition of the Hertz vector Eq. A.19. The scattered electric field is related to the scattered displacement vector by $\mathbf{D}_s = \varepsilon_o\mathbf{E}_s$, where ε_o is the dielectric constant at the detector position $\mathbf{R}$. Thus, $\mathbf{E}_s$ is

$$\mathbf{E}_s(R,t) = \nabla\times\nabla\times\frac{E_0}{4\pi\varepsilon_o}\int_V d^3r\frac{1}{|\mathbf{R}-\mathbf{r}|}(\delta\underline{\varepsilon}(\mathbf{r},t')\cdot\hat{\mathbf{n}}_i)\exp i(\mathbf{k}_i\cdot\mathbf{r}-\omega_i t') \ . \tag{A.24}$$

The detector will be assumed to be very far away from the scattering medium, such that $\mathbf{R}$ dominates $\mathbf{r}$. Therefore $|\mathbf{R}-\mathbf{r}|$ may be expanded as a binomial power series

$$|\mathbf{R}-\mathbf{r}| \cong R - \mathbf{r}\cdot\hat{\mathbf{k}}_f + \ldots \tag{A.25}$$

where $\hat{\mathbf{k}}_f$ is a unit vector in the direction of $\mathbf{R}$. Thus, to a good approximation, the retarded time t' is

$$t' \cong t - \frac{\sqrt{\varepsilon}}{c}\left(R - \mathbf{r}\cdot\hat{\mathbf{k}}_f\right) \ . \tag{A.26}$$

Now, let us do a Fourier analysis of $\delta\underline{\varepsilon}(\mathbf{r},t')$ over a time interval T

$$\delta\underline{\varepsilon}(\mathbf{r},t') = \sum_p \delta\underline{\varepsilon}_p(\mathbf{r})\exp i\Omega_p t' \ , \tag{A.27}$$

where $\Omega_p = (2\pi/T)p$, the frequency components of the Fourier decomposition. The only components Ω_p that contribute significantly to this sum are those that correspond to the natural frequencies of rotation and translation of the system. These frequencies are less than 10^{13} Hz, which is much smaller than the frequency of the incident light, ω_i which is on the order of 10^{14} Hz, i.e., $\omega_i \gg \Omega_p$ for all significant Ω_p. Equations A.26 and A.27 are now substituted into Eq. A.24

$$\mathbf{E}_s = \nabla\times\nabla\times\frac{E_o}{4\pi\varepsilon_o}\sum_p\int_V d^3r\frac{1}{|\mathbf{R}-\mathbf{r}|}\delta\underline{\varepsilon}(\mathbf{r})\cdot\hat{\mathbf{n}}_i\exp(i\Omega_p t)\exp i(\mathbf{k}_i\cdot\mathbf{r}-\omega_i t)$$
$$\exp\left[(\omega_i-\Omega_p)\frac{\sqrt{\varepsilon}}{c}R - (\omega_i-\Omega_p)\frac{\sqrt{\varepsilon}}{c}\mathbf{r}\cdot\hat{\mathbf{k}}_f\right] \tag{A.28}$$

Eq. A.28 can be simplified somewhat by defining the relations $\omega_f \equiv \omega_i - \Omega_p$ and $\mathbf{k}_p \equiv (\sqrt{\varepsilon}/c)\omega_f \hat{\mathbf{k}}_f$. Using these relations, Eq. A.28 becomes

$$\mathbf{E}_s = \boldsymbol{\nabla}\times\boldsymbol{\nabla}\times\frac{E_o}{4\pi\varepsilon_o}\sum_p e^{-i\omega_i t}\cdot\int_V d^3r\frac{1}{|\mathbf{R}-\mathbf{r}|}\delta\underline{\varepsilon}(\mathbf{r})\cdot\hat{\mathbf{n}}_i e^{i\Omega_p t}e^{(\mathbf{k}_i-\mathbf{k}_p)\cdot\mathbf{r}}e^{ik_pR} . \quad (A.29)$$

Next, we notice that the curls of the integral are taken with respect to $\mathbf{R}$, not $\mathbf{r}$, so that they can be taken inside the integral. Furthermore, we will discard all terms of order greater than $(1/R)$. Effectively, this means that all of the derivatives of the $1/|\mathbf{R}-\mathbf{r}|$ factor are neglected, as they are necessarily of order $1/R^2$ or higher. Pulling the $1/|\mathbf{R}-\mathbf{r}|$ factor out of the double curl and approximating it by $1/R$, the scattered field is

$$\mathbf{E}_s = \frac{E_o}{4\pi\varepsilon_o R}\sum_p e^{-i\omega_i t}\int_V d^3r e^{i\Omega_p t}e^{i((\mathbf{k}_i-\mathbf{k}_p)\cdot\mathbf{r}}\boldsymbol{\nabla}\times\boldsymbol{\nabla}\times\delta\underline{\varepsilon}(\mathbf{r})\cdot\hat{\mathbf{n}}_i e^{ik_pR} . \quad (A.30)$$

The curls in Eq. A.30 can be dealt with using the vector identity

$$\boldsymbol{\nabla}\times\mathbf{A}(\exp i\mathbf{k}\cdot\mathbf{r}) = i\mathbf{k}\times\mathbf{A}(\exp i\mathbf{k}\cdot\mathbf{r}) . \quad (A.31)$$

Using this identity simplifies Eq. A.30 to

$$\mathbf{E}_s = \frac{E_o}{4\pi\varepsilon_o R}\sum_p e^{i(k_pR-\omega_i t)}\mathbf{k}_p\times\mathbf{k}_p\times\int_V d^3r e^{i(\mathbf{k}_i-\mathbf{k}_p)\cdot\mathbf{r}}\delta\underline{\varepsilon}(\mathbf{r})\cdot\hat{\mathbf{n}}_i e^{i\Omega_p t} . \quad (A.32)$$

Since $\Omega_p \ll \omega_i$, k_p is, to a good approximation,

$$k_p \cong \frac{\sqrt{\varepsilon}}{c}\omega_i = k_i \cong k_f , \quad (A.33)$$

where $\omega_i = ck_i/n$ and $n = \sqrt{\varepsilon}$ is the local index of refraction.[1] Therefore, it can seen that $k_p\hat{\mathbf{k}}_f \cong k_i\hat{\mathbf{k}}_f = \mathbf{k}_f$ (cf. Fig. 2.2)[2]. The only p-dependent quantities left in the sum are $\delta\underline{\varepsilon}$ and $e^{i\Omega_p t}$, so the sum can be evaluated using Eq. A.27

$$\mathbf{E}_s = \frac{E_o}{4\pi\varepsilon_o R}e^{i(k_fR-\omega_i t)}\int_V d^3r e^{i\mathbf{q}\cdot\mathbf{r}}\mathbf{k}_f\times\mathbf{k}_f\times(\delta\underline{\varepsilon}(\mathbf{r},t)\cdot\hat{\mathbf{n}}_i) , \quad (A.34)$$

[1] It is important to note that this is the index of refraction *in the medium*, where the scattering takes place. Normally, this fact is neglected in derivations of the scattered field (but not by experimentalists!).

[2] Remember that k_p is a mathematical construct, originating in the Fourier transform in Eq. A.27.

where $\mathbf{q} = \mathbf{k}_i - \mathbf{k}_f$ is the scattering vector.

It should be noted that $k_f = k_i$ and the definitions of $\mathbf{q}$ and $\mathbf{k}_f$ are consistent with Fig. 2.2 and with Eq. 2.6. Also, Eq. A.34 depends only on the real time t and not the retarded time t'.

Taking the component of $\mathbf{E}_s$ in the direction of polarization of the scattered field $\mathbf{n}_f$ gives

$$E_s(R,t) = \frac{E_o}{4\pi\varepsilon_o R} \exp i(k_f R - \omega_i t) \int_V d^3r e^{i\mathbf{q}\cdot\mathbf{r}} \mathbf{n}_f \cdot [\mathbf{k}_f \times \mathbf{k}_f \times [\delta\underline{\varepsilon}(\mathbf{r},t)\cdot\hat{\mathbf{n}}_i]] \ , \quad \text{(A.35)}$$

which this the same as Eq. 2.5.

It is important to remember that this and all other results given in this thesis assume that the incident light wave is scattered only once. Multiple scattering is the result of terms in $\delta\underline{\varepsilon}$ of greater than first order, which have been neglected after Eq. A.15.

Appendix B

Form Factor of a Hollow Shell

As an example, we will derive the form factor $P(\mathbf{q})$ of a hollow sphere with a finite thickness starting from Eq. 2.15:

$$P(\mathbf{q}) = \left\langle \left| \frac{1}{\ell} \sum_{j=1}^{\ell} e^{i\mathbf{q}\cdot\mathbf{r}_j} \right|^2 \right\rangle . \tag{B.1}$$

The inner and outer radii of the shell are R_i and R_o, respectively.

The first step is to convert Eq. 2.15 from a summation to an integral form. Since the problem obviously has spherical symmetry, we convert the summation to an integral in spherical coordinates over the volume of the sphere. Noting that the summation is normalised by the factor of $1/\ell^2$, we normalise by dividing by an integral over the same volume. The form factor is now given by

$$\begin{aligned} P(\mathbf{q}) &= \left| \frac{\int_{\theta=0}^{\pi} d\theta \sin\theta \int_{\phi=0}^{2\pi} \int_{r=R_i}^{R_o} dr\, r^2 e^{i\mathbf{q}\cdot\mathbf{r}}}{\int_{\theta=0}^{\pi} d\theta \sin\theta \int_{\phi=0}^{2\pi} \int_{r=R_i}^{R_o} dr\, r^2} \right|^2 \\ &= \left| \frac{2\pi \int_{\theta=0}^{\pi} d\theta \sin\theta \int_{r=R_i}^{R_o} dr\, r^2 e^{iqr\cos\theta}}{4\pi \int_{r=R_i}^{R_o} dr\, r^2} \right|^2 \\ &= \left(\frac{3}{R_o^3 - R_i^3} \int_{r=R_i}^{R_o} dr\, r^2 \frac{\sin qr}{qr} \right)^2 . \end{aligned} \tag{B.2}$$

Equation B.2 can be integrated by parts to obtain

$$P(\mathrm{q}) = \left[\left(\frac{3}{q^3 t^3}\right)(\sin qR_o - qR_o \cos qR_o - \sin qR_i + qR_i \cos qR_i)\right]^2 . \qquad \text{(B.3)}$$

Note that it is unnecessary to average over all angles due to the spherical symmetry. If this were not so, a second integration over the total solid angle would be required.

Appendix C

Extrusion by Vesicle Deflation

As an alternative to rupturing a vesicle at the entrance to a pore and expelling the contents, we will consider the possibility that water instead flows out of the vesicle more quickly than it flows in, decreasing the vesicle's volume and allowing it to enter the pore without rupturing. If the functional form of the rate of outflow of water is known, the time required to forcibly decrease the vesicle's volume by the necessary amount can be determined by integration. The time required to extrude the entire 5 mℓ sample in this fashion is then also easily calculated.

For a quasi-stationary membrane exposed to both a hydrostatic pressure $\delta P = P_{in} - P_{out}$ and an osmotic pressure difference $\delta\Pi = \Pi_{in} - \Pi_{out}$, the solvent volume current J is given by

$$J = \Lambda\,(\delta P \; - \; \delta\Pi) \;, \tag{C.1}$$

where Λ is the permeability of the membrane. We must be careful to note here that Λ is actually proportional to the area of the appropriate section of membrane, and will therefore be different for the volume current into and out of the vesicle.

Let us consider the situation shown in Fig. 5.2. In addition to the quantities shown, let the concentrations of osmolytes below, above and inside the vesicle be given by C_0, C_1 and C_2, respectively. These can be changed to osmotic pressures by multiplying them by R_gT, where $R_g = 8.3143$ J/mol·K and T is the temperature in kelvins. The portion of the vesicle inside and outside the pore will be referred to by the subscripts o and i, respectively. This leads to two equations for the volume current across the

two sections of the vesicle

$$J_o = \Lambda_o \left[(P_2 - P_0) - R_g T \left(C_2 - C_0 \right) \right] \text{ , and} \tag{C.2}$$

$$J_i = \Lambda_i \left[(P_2 - P_1) - R_g T \left(C_2 - C_1 \right) \right] . \tag{C.3}$$

The two permeabilities Λ_i and Λ_o will be expressed as the product of the appropriate area with a constant factor λ, such that

$$\Lambda_i = \lambda A_i = \lambda \left(A - A_o \right) \text{ , and} \tag{C.4}$$

$$\Lambda_o \ \lambda A_o . \tag{C.5}$$

where A is the total area of the vesicle. By their definitions, these volume currents are positive for flow into the vesicle. The total rate of change of volume J of the vesicle is given by the sum of these two volume currents

$$J = J_o + J_i . \tag{C.6}$$

Substituting the definitions of J_i and J_o in Eq. C.6 and simplifying, and noting that the concentrations C_0 and C_1 are equal gives

$$J = \lambda \left(A \left[(P_2 - P_1) - R_g T \left(C_2 - C_1 \right) \right] + A_o \left(P_1 - P_0 \right) \right) . \tag{C.7}$$

We will approximate the pressure difference $P_2 - P_1$ across the upper portion of the vesicle by the Laplace pressure $2\gamma/R$, and assume that neither this pressure nor the area of the vesicle across which water can flow is changing.

Next, we note that we are considering solvent concentrations, not solute concentrations. The exterior concentration C_1 is constant and the interior concentration C_2 is very nearly so. The result is that the term in Eq. C.7 involving the concentrations is negligible. All of the remaining terms are constant, so that we have

$$J = \lambda \left(A_o (P_1 - P_0) + A \frac{2\gamma}{R} + R_g T A C_1 \right) \tag{C.8}$$

The time rate of change of the volume of the vesicle dV/dt is by definition the volume current J. The time required for a change of volume from V_1 to V_2 is found by integrating, which of course yields a function inversely proportional to J.

$$t = \frac{V_2 - V_1}{J} \tag{C.9}$$

Now some assumptions must be made about numerical values used to evaluate Eq. C.9. We will consider the situation where DMPC vesicles with a mean radius R of 1 μm are extruded at 30 psi and 30°C. The pressure difference $P_1 - P_0$ is equal to the pressure drop of 30 psi. The surface tension will be taken to be 4.2×10^{-3} N/m, equal to the lysis tension shown in Table 5.3. We also need to know something about λ. The flux permeability $\mathcal{P}$ of egg PC membranes to water is 2×10^{-6} m/s [60]. From these values we find that $\lambda = 1.43 \times 10^{-14}$ m^4/J -s.

The initial volume of the vesicle V_1 is effectively $\frac{4}{3}\pi R^3 = 4.19 \times 10^{-18}$ m^3, the volume of the small portion inside the pore being negligible. The final vesicle is assumed to be a spherocylinder of the same area as the initial vesicle and having a radius r equal to that of the pore, which in this case is 50 nm. The volume of this spherocylinder is $V_2 = 3.14 \times 10^{-19}$ m^3. The volume of the whole vesicle A is $4\pi R^2 = 1.26 \times 10^{-11}$m^2 and the area of the vesicle inside the pore is $A_o = 2\pi r^2 = 1.57 \times 10^{-14}$m^2.

With these areas and the values above, we find that $J = 1.55 \times 10^{-21}$m^3/s. This result is dominated by the term involving the surface tension. The time to change the vesicle volume from V_1 to V_2 is

$$t = \frac{V_2 - V_1}{J} = \frac{-3.88 \times 10^{-18} \text{ m}^3}{1.55 \times 10^{-21} \text{ m}^3/\text{s}} = 2500 \text{ s} \simeq 42 \text{ min} . \qquad \text{(C.10)}$$

The result is negative due to our definition of J as being positive for net flow into the vesicle. If we had defined J such that it was positive for net outflow from the vesicle the time would have been positive. Forty-two minutes are required to deflate a vesicle enough so that it will fit through the pore. A typical 5 mℓ vesicle solution has 8.84×10^{10} vesicles suspended in it, while there are around 1.66×10^9 pores on a membrane surface. This means that an average of 53 vesicles must pass through each pore. It would take about 37 hours to push all of the vesicles through the membrane under these conditions. It is observed experimentally that vesicles pass through the filter in a fraction of this time, implying that permeation of the membrane is not a significant factor in extruding vesicles.

Bibliography

[1] M.J. Hope, M.B. Bally, G. Webb and P.R. Cullis, "Production of large unilamellar vesicles by a rapid extrusion procedure: characterization of size, trapped volume and ability to maintain a membrane potential," Biochim. Biophys. Acta. **812**, 55-65 (1985).

[2] R.C. MacDonald, R.I. MacDonald, B.Ph.M. Menco, K. Takeshita, N.K. Subbarao and L. Hu, "Small-volume extrusion apparatus for preparation of large, unilamellar vesicles," Biochim. Biophys. Acta. **1061**, 297-303 (1993).

[3] S.G. Clerc and T.E. Thompson, "A possible mechanism for vesicle formation by extrusion," Biophys. J. **67**, 475-477 (1994).

[4] G. Gompper, and D.M. Kroll, "Driven transport of fluid vesicles through narrow pores," Phys. Rev. E. **52**, 4198-4208 (1995).

[5] R. Bruinsma, "Rheology and shape transitions of vesicles under capillary flow," Physica A **234**, 249-270 (1996).

[6] M. Kraus, W. Wintz, U. Seifert and R. Lipowsky, "Fluid vesicles in shear flow," Phys. Rev. Lett **77**, 3685-3688 (1996).

[7] J. Vanderlinde, *Classical Electromagnetic Theory*, (John Wiley & Sons, New York, 1993).

[8] C.S. Johnson, Jr. and D.A. Gabriel, *Laser Light Scattering*, (Dover Publications, New York, 1994).

[9] B.J. Berne and R. Pecora, *Dynamic Light Scattering*, (Robert E. Krieger Publishing Company, Florida, 1976)

[10] K.B. Strawbridge and F.R. Hallett, "Polydisperse Mie theory applied to hollow latex spheres: An integrated light-scattering study," Can. J. Phys. **70**, 401-406 (1992).

[11] V. Digiorgio and J.B. Lastovka, "Intensity-Correlation Spectroscopy," Phys. Rev. A **4**, 2033-2050 (1971).

[12] D.E. Koppel, "Analysis of macromolecular polydispersity in intensity correlation spectroscopy: the method of cumulants," J. Chem. Phys. **57**, 4814-4820 (1972).

[13] W.H. Press, S.A. Teukolsky, W.T. Vetterling, and B.P. Flannery, *Numerical Recipes in C: the art of scientific computing*, 2nd ed., (Cambridge University Press, Cambridge, 1992).

[14] J. Israelachvili, *Intermolecular & Surface Forces*, (Academic Press, San Diego, 1992).

[15] C. Tanford, *The Hydrophobic Effect: Formation of Micelles and Biological Membranes*, 2nd. Ed., (John Wiley & Sons, New York, 1980).

[16] S.A. Safran, *Statistical Thermodynamics of Surfaces, Interfaces and Membranes*, (Addison-Wesley Publishing Company, 1994).

[17] P.G. de Gennes and J. Prost, *The Physics of Liquid Crystals*, 2nd. Ed., (Oxford University Press, New York, 1993).

[18] C. Tanford, "Hydrostatic pressure in small phospholipid vesicles," Proc. Natl. Acad. Sci. USA **76**, 3318-3319 (1979).

[19] U. Seifert, "The concept of effective tension for fluctuating vesicles," Z. Phys. B **97**, 299-309 (1994).

[20] M. Bloom, E. Evans and O.G. Mouritsen, "Physical properties of the fluid lipid-bilayer component of cell membranes: a perspective," Quart. Rev. Biophys **24**, 293-397 (1991).

[21] E. Evans and W. Rawicz, "Entropy-driven tension and bending elasticity in condensed-fluid membranes," Phys. Rev. Lett. **64**, 2094-2097 (1990).

[22] E.A. Evans, "Bending resistance and chemically induced moments in membrane bilayers," Biophys. J. **14**, 923-931 (1974).

[23] E. Evans and R. Skalak, "Mechanics and thermodynamics of membranes," CRC Crit. Rev. Bioeng. **3**, 181-418 (1980).

[24] E. Evans and R. Kwok, "Mechanical calorimetry of large dimyristoylphosphatidylcholine vesicles in the phase transition region," Biochem. **21**, 4874-4879 (1982).

[25] E. Evans and D. Needham, "Physical properties of surfactant bilayer membranes: Thermal transitions, elasticity, rigidity, cohesion and colloidal interactions," J. Phys. Chem. **91**, 4219-4228 (1987).

[26] D. Needham, T.J. McIntosh and E. Evans, "Thermomechanical and transition properties of dimyristoylphosphatidylcholine/cholesterol bilayers," Biochem. **27**, 4668-4673 (1988).

[27] D. Needham and E. Evans, "Structure and mechanical properties of giant lipid (DMPC) vesicle bilayers from 20°C below to 10°C above the liquid crystal-crystalline phase transition at 20°C," Biochem **27**, 8261-8269 (1988).

[28] D. Needham and R.S. Nunn, "Elastic deformation and failure of lipid bilayer membranes containing cholesterol," Biophys. J. **58**, 997-1009 (1990).

[29] W. Helfrich, "Elastic properties of lipid bilayers: Theory and possible experiments," Z. Naturforsch. **28**, 693-703.

[30] H.P. Duwe, J. Kaes and E. Sackmann, "Bending elastic moduli of lipid bilayers: modulation by solutes," J. Phys. France **51**, 945-962 (1990).

[31] D.J. Bukman, J.H. Yao and M. Wortis, "Stability of cylindrical vesicles under axial tension," Phys. Rev. E **54**, 5463-5468 (1996).

[32] W. Rawicz, private communication (1996).

[33] J.C. Shillcock and D.H. Boal, "Entropy-driven instability and rupture of fluid membranes," Biophys. J. **71**, 317-326 (1996)

[34] B.L.-S. Mui, P.R. Cullis, E.A. Evans and T.D. Madden, "Osmotic properties of large unilamellar vesicles prepared by extrusion," Biophys. J. **64**, 443-453 (1993).

[35] A. Ertel, G. Marangoni, J. Marsh, F.R. Hallett and J.M. Wood, "Mechanical properties of vesicles. I. Coordinated analysis of osmotic swelling and lysis," Biophys. J. **64**, 426-434 (1993).

[36] Y. Kagawa and E. Racker, "Partial resolution of the enzymes catalyzing oxidative phosphorylation," J. Biol. Chem. **246**, 5477-5487 (1971).

[37] J. Bruner, P. Skrabal and H. Hauser, 1"Single bilayer vesicles prepared without sonication: Physico-chemical properties," Biochim. Biophys. Acta **455**, 322-332 (1976).

[38] H.G. Enoch and P. Strittmatter, "Formation and properties of 1000-Å-diameter, single-bilayer phospholipid vesicles," Proc. Natl. Acad. Sci. USA **76**, 145-149 (1979).

[39] F. Szoka and D. Papahadjopoulos, "Procedure for preparation of liposomes with large internal aqueous space and high capture by reverse-phase evaporation," Proc. Natl. Acad. Sci. USA **79**, 4194-4198 (1978).

[40] D.W. Deamer and A.D. Bangham, "Large volume liposomes by an ether vaporization method," Biochim. Biophys. Acta **443**, 629-634 (1976).

[41] C.H. Huang, "Studies on phosphatidylcholine vesicles: Formation and physical characteristics," Biochemistry **8**, 344-352 (1969).

[42] L.D. Mayer, M.J. Hope and P.R. Cullis, "Vesicles of variable sizes produced by a rapid extrusion procedure," Biochim. Biophys. Acta. **858**, 161-168 (1986).

[43] R. Nayer, M.J. Hope and P.R. Cullis, "Generation of large unilamellar vesicles from long-chain saturated phosphatidylcholines by extrusion techniques," Biochim. Biophys. Acta. **986**, 200-206 (1989).

[44] S., Kölchens, V. Ramaswami, J. Birgenheier, L. Nett and D.F. O'Brien, "Quasi-elastic light scattering determination of the size distribution of extruded vesicles," Chem. Phys. Lipids **65**, 1-10 (1993).

[45] L.D. Landau and E. Lifshitz, *Fluid Mechanics*, 2nd Ed. (Pergamon Press, Oxford, 1987).

[46] P. Walstra, *Encyclopedia of Emulsion Technology*, Vol. 1, Ed. P. Becher (Marcel Dekker, Inc., New York, 1983).

[47] J.W. Strutt, Lord Rayleigh, "On the Instability of Jets," Proc. London Math. Soc. **X**, 4-13 (1879).

[48] R. Bar-Ziv and E. Moses, "Instability and "pearling" states produced in tubular membranes by competition of curvature and tension," Phys. Rev. Lett. **73**, 1392-1395 (1994).

[49] G. Gompper, private communication (1996).

[50] F.P. Bretherton, "The motion of long bubbles in tubes," J. Fluid Mech. **10**, 166-188 (1961).

[51] H.L. Goldsmith and S.G. Mason, "The motion of single large bubbles in closed vertical tubes," J. Fluid Mech. **14**, 42-58 (1962).

[52] A.C.L. Barnard, L. Lopez and J.D. Hellums, "Basic theory of blood flow in capillaries," J. Microvasc. Res. **1**, 23-34 (1968).

[53] L. Pauling, *General Chemistry*, 3rd. Ed. (Dover Publications, Mineola, NY, 1988).

[54] L.D. Mayer, M.J. Hope, P.R. Cullis and A.S. Janoff, "Solute distributions and trapping efficiencies obsrved in freeze-thawed multilamellar vesicles," Biochim. Biophys. Acta **817**, 193-196 (1985).

[55] C. Asman, private communication (1997).

[56] E. Lau, S.F.U. M.Sc. Thesis (1994).

[57] T.G. Mason and J. Bibette, "Emulsification of Viscoelastic Media," Phys. Rev. Lett. **77**, 3481-3484 (1996).

[58] O. Diat, D. Roux, and F. Nallet, "Effect of shear on a lyotropic lamellar phase," J. Phys. II **3**, 1427-1452 (1993).

[59] L.D. Landau and E. Lifshitz, *Electrodynamics of Continuous Media*, 2nd Ed., rev. and enl. (Pergamon Press, Oxford, 1984).

[60] R.B. Gennis, *Biomembranes: molecular structure and function*(Springer-Verlag, New York, 1989).

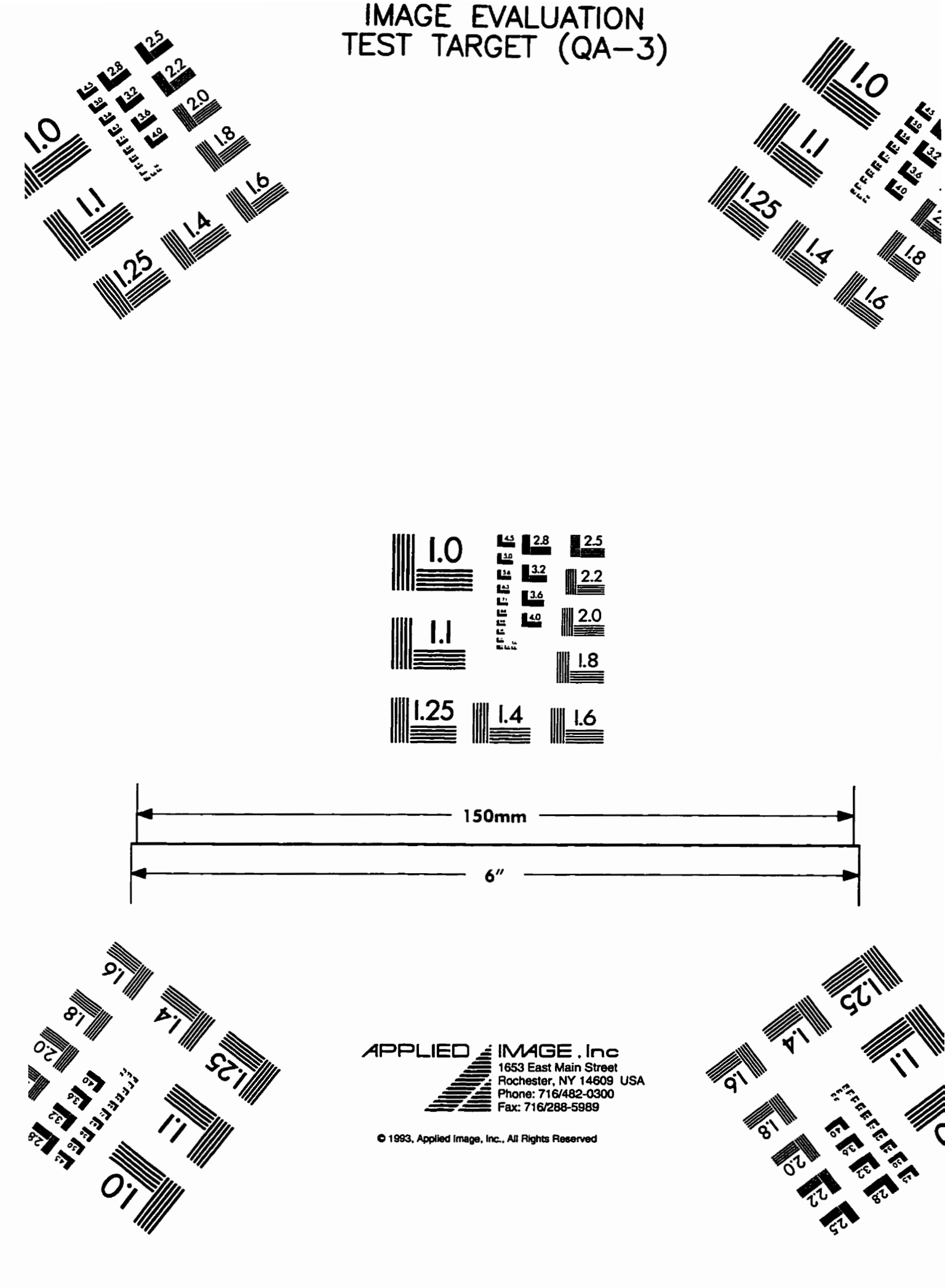
IMAGE EVALUATION
TEST TARGET (QA-3)
1.0
1.1
1.25
1.4
1.6
1.8
2.0
2.2
2.5
2.8
3.2
3.6
4.0
150mm
6"
APPLIED IMAGE, Inc
1653 East Main Street
Rochester, NY 14609 USA
Phone: 716/482-0300
Fax: 716/288-5989
© 1993, Applied Image, Inc., All Rights Reserved